Final Report

Research Project No.:	03SX202A
Project Title:	Investigation of higher order pressure fluctuations and its influence on ship stern, taking into account cavitation at propeller blades

Authors: Dr. Conxita Lifante,
Dr. Thomas Frank

Performing Organisation: ANSYS Germany GmbH
Staudenfeldweg 12
D-83624 Otterfing
Germany

Publication Date: 18. December 2008

Report-No.: **ANSYS / TR-08-04**

Abschlussbericht

Förderkennzeichen.: 03SX202A

Vorhabensbezeichnung: Untersuchung der Druckschwankungen höherer Ordnung am Hinterschiff unter Berücksichtigung der Kavitation am Propeller

Autoren: Dr. Conxita Lifante,
PD Dr.-Ing. habil. Thomas Frank

Dienststelle des Autors: ANSYS Germany GmbH
Staudenfeldweg 12
D-83624 Otterfing
Germany

Berichtsdatum: 18. Dezember 2008

Berichtsnummer: **ANSYS / TR-08-04**

Document Control Sheet

1. ISBN or ISSN	2. type of document (e.g. report, publication) Final Report
3. title Investigation of higher order pressure fluctuations and its influence on ship stern, taking into account cavitation at propeller blades	
4. author(s) (family name, first name(s)) Lifante, Conxita; Frank, Thomas	5.end of project 30.06.2008
	6. publication date 18. December 2008
	7. form of publication Booklet
8. performing organization(s) (name, address) ANSYS Germany GmbH Staudenfeldweg 12 83624 Otterfing	9. originator's report no. ANSYS / TR-08-04
	10. reference no. 03SX202A
	11. no. of pages 69
13. sponsoring agency (name, address) Bundesministerium für Bildung und Forschung (BMBF) 53170 Bonn	12. no. of references 38
	14. no. of tables 6
	15. no. of figures 50
16. supplementary notes	
17. presented at (title, place, date)	

18. abstract

The onset of cavitation around propellers or other ship components leads to reduction of performance, erosion, vibrations and noise among other drawbacks. Experimental investigations of the cavitation induced pressure oscillations are both very time consuming and expensive. Therefore, to be able to simulate accurately such behaviour and to optimize new designs is an important demand from the side of shipbuilding industry. CFD simulations allow to save time and costs and to improve the quality of this kind of ship components.

However, the description of cavitation in the context of a numerical flow simulation is a complex task, which requires specific model developments, experimental investigations of generic and application-oriented testcases, and validation of the numerical results against them.

This was exactly the goal of the current research project and the methodology applied during its execution. The aim of the investigations performed was the study of the pressure oscillations induced by cavitation taking place at the blades of a P1356 propeller A model to deal with cavitation has been developed in ANSYS CFX. It has been validated by comparison to three different testcases: a 2D hydrofoil configuration, a 3D hydrofoil configuration and the P1356 propeller. The first two cases are well known cases, and experimental data are available in literature, while the experimental data of the propeller P1356 was provided by the project partner Schiffbau Versuchsanstalt Potsdam (SVA). SVA operates a cavitation tunnel, where different experimental studies were carried out. Transient pressure signals recorded on a transducer plate as well as high-speed video showing the cavitation pattern were used for validation purposes. In numerical simulation strong influence of the grid resolution and turbulence modelling was found in solving the strong swirling flows involved in such propeller flow configurations. A satisfactory agreement between the numerical investigations and the experimental data was obtained for all three testcases, evidencing the appropriateness of the modelling in ANSYS CFX to deal with complex marine applications.

19. keywords CFD, modelling, multiphase flow, turbulence, cavitation, validation, marine applications, hydrofoil, propeller, rotor-stator	
20. publisher	21. price

Berichtsblatt

1. ISBN oder ISSN	2. Berichtsart (Schlussbericht oder Veröffentlichung) Abschlussbericht
3. Titel Untersuchung der Druckschwankungen höherer Ordnung am Hinterschiff unter Berücksichtung der Kavitation am Propeller	
4. Autor(en) [Name(n), Vorname(n)] Lifante, Conxita; Frank, Thomas	5. Abschlussdatum des Vorhabens 30.06.2008
	6. Veröffentlichungsdatum 18. Dezember 2008
	7. Form der Publikation Broschüre
8. Durchführende Institution(en) (Name, Adresse) ANSYS Germany GmbH Staudenfeldweg 12 83624 Otterfing	9. Ber. Nr. Durchführende Institution ANSYS / TR-08-04
	10. Förderkennzeichen *) 03SX202A
	11. Seitenzahl 69
13. Fördernde Institution (Name, Adresse) Bundesministerium für Bildung und Forschung (BMBF) 53170 Bonn	12. Literaturangaben 38
	14. Tabellen 6
	15. Abbildungen 50
16. Zusätzliche Angaben	
17. Vorgelegt bei (Titel, Ort, Datum)	

18. Kurzfassung

Der Einsatz von Kavitation an Propellern oder anderen Schiffsbauteilen führt zu einer Leistungsminderung, Kavitationserosion, Vibrationen und neben anderen Nachteilen auch zu Lärm. Experimentelle Untersuchungen derartiger kavitationsinduzierter Druckoszillationen ist sowohl zeitaufwändig als auch kostenintensiv. Daher ist es von Seiten der Schiffbauindustrie sehr wünschenswert, derartige Untersuchungen und Design-Optimierungen mit hoher Genauigkeit auf der Basis von CFD-Simulationen ausführenzu können. CFD-Simulationen helfen hier, Zeit und Kosten zu sparen und die Qualität derartiger Schiffsbaukomponenten zu verbessern. Die Beschreibung von Kavitation im Kontext einer numerischen Strömungssimulation ist jedoch eine komplexe Aufgabenstellung, die experimentelle Untersuchungen von generischen und anwendungsorientierten Testfällen und die Validierung von CFD-Modellen im Vergleich mit diesen Experimenten erfordern.
Hierin bestand das wesentliche Ziel des vorliegenden Forschungsvorhabens. Das Ziel der Untersuchungen bestand in der Berechnung der kavitationsinduzierten Druckoszillationen ausgehend von den Blättern eines P1356 Fahrgastschiff-Propellers. Hierbei wurde ein in ANSYS CFX entwickeltes Kavitationsmodell eingesetzt. Dieses Kavitationsmodell wurde an drei ausgewählten Testfällen validiert: ein 2d Hydrotragflügel, ein 3d Hydrotragflügel und letztendlich die Konfiguration des P1356 Propellers. Bei den ersten beiden Fällen handelt es sich um aus der Literatur entnommene Testfälle, während die Experimente für den P1356 Propeller vom Projektpartner Schiffsbau-Versuchsanstalt, Potsdam (SVA) ausgeführt wurden. Hierfür betreibt die SVA Potsdam einen Kavitationstunnel, an die verschiedenen Experimente ausgeführt wurden. Zum Vergleich mit den CFD-Simulationen wurden transiente Drucksignale aufgenommen sowie High-Speed Video-Aufnahmen vom Kavitationsbild am Schiffspropeller gemacht. Die numerischen Untersuchungen haben den großen Einfluss einer hohen Gitterauflösung und der Turbulenzmodellierung auf das Simulationsergebnis gezeigt. Für alle drei Testfälle konnte in sorgfältigen Untersuchungen eine gute Übereinstimmung mit den Experimenten erzielt werden, womit die Genauigkeit der physikalischen Modellierung in ANSYS CFX in Schiffbau-technischen Anwendungen unter Beweis gestellt werden konnte.

19. Schlagwörter
CFD, Modellierung, Mehrphasenströmung, Turbulenz, Kavitation, Validierung, Schiffbau, Tragflügel, Propeller, Rotor-Stator

20. Verlag	21. Preis

*) Auf das Förderkennzeichen des BMBF soll auch in der Veröffentlichung hingewiesen werden.

BMBF-Vordr. 3831/03.07

Contents

Figure List

Table List

1. Acknowledgement

The underlying research project of this final report has been funded by the German Ministry of Education and Research (BMBF) under the grant No. 03SX202A. The authors of this report are fully responsible for the contents of this publication.

Das diesem Bericht zugrundeliegende Vorhaben wurde mit Mitteln des Bundesministeriums für Bildung und Forschung (BMBF) unter dem Förderkennzeichen 03SX202A gefördert. Die Verantwortung für den Inhalt dieser Veröffentlichung liegt bei den Autoren.

2. Introduction

Equation Section 1

The onset of cavitation around propellers, hydrofoils, ships, etc represents an important issue in terms of reduced performance, erosion and passenger/crew comfort due to cavitation induced vibrations and noise among other drawbacks. The accurate prediction of such phenomena stands increasingly in the interest of the ship manufacturers, the shipyards, classification societies, etc. The size of the propeller induced pressure fluctuations is a quality criterion for any design and leads to the dimensioning of the ship structures. Already in the designing phase their maximum values are defined. Consequently cavitation has been studied by many researchers, but up to now most of the investigations are still experiments. Experimental investigations of the pressure oscillations induced by the propeller at the rear part of the ship are very time-consuming and expensive. There is, therefore, on part of the shipbuilding industry the requirement to seize the propeller effects by numerical CFD[1] simulations in order to save time and costs during the construction of the ships and to increase the quality of their designs at the same time.

In addition, uncertainties in the upscaling from the experimental data to real scale designs appear. There is, therefore, on the part of the marine industry a demand to analyze the propeller effects using CFD. In this case, many different real scale numerical prototypes can be investigated. The exponential increase of computational speed and memory resources of the computers/work stations/clusters in the last years, combined with the decrease of the price of such equipments, had an enormous impact on the scientific community. The use of CFD tools is everyday more and more popular in order to perform many investigations. The hardware evolution shows the same trends for the near future. Therefore, even finer grids can be employed, as well as more phenomena can be studied simultaneously.

The description of the cavitation in the context of a numerical flow simulation is a complex task, which requires specific model developments, experimental investigations of generic and application-oriented testcases as well as comparison between them in order to improve those models.

Cavitation is caused when the local pressure falls below the vapour pressure. This drop in local pressure below vapour pressure can be caused by geometrical design, leading to local pressure minima. On the other hand side there is the phenomena of turbulence induced cavitation. So the tip vortices departing from propeller blades play an important role in the prediction of cavitation. Due to the high circumferential velocity values in tip vortices, there is a drop of the pressure in the vortex core, which can lead to the inception of cavitation. Therefore an important point in order to predict cavitation is the accurate resolution of the design and turbulence induced pressure oscillations taking place at the propeller. The flow around propellers usually has high Reynolds number, and this means it is turbulent. Therefore, the turbulence modelling plays an important role as well.

[1] CFD – Computational Fluid Dynamics

Until a few years ago flows around propellers were solved by using a k-ε two equation turbulence modelling with logarithmic wall functions. It is known that this approach has some disadvantages. Thus, the aeronautic or marine industry has applied intensively the SST approach. This consists of a combination of k-ε and k-ω models where a modified eddy viscosity approach is applied. In this way the accuracy of the solution is improved.

In addition the wall treatment was also improved. The most successful development are the so called automatic wall functions. In this manner the shear stress at the wall is computed using a linear or a logarithmic profile depending on the wall distance of the first grid point. This strategy improves the accuracy of the numerical solution.

The SST model was used in the present work as the first turbulence model approach. However, as well as other 2-equation turbulence models it is an isotropic method, and therefore it is not adequate to predict the effects of the strong curvature of the streamlines in such flows. Therefore, the so-called Reynolds Stress models were also analyzed showing improved results. In this case, transport equations for all 6 independent components of the Reynolds Stress tensor are solved. On the other hand, this increased numerical effort increases the CPU time and memory resources needed for the flow simulation. Finally, the most accurate simulations were performed by means of Scale-Adaptive or Detached Eddy Simulation (SAS or DES), which are able to resolve the large turbulent structures while modelling the isotropic sub-grid scale turbulence.

A model to deal with cavitation and the pressure fluctuations introduced by it has been developed in ANSYS CFX[3], and the corresponding validation of it has been carried out. Different test cases have been chosen for this purpose:

- 2D case consisting of a plano-convex hydrofoil profile, where cloud cavitation can be observed.
- 3D case, where the fluid flows around a NACA 66_2-415 hydrofoil. A tip vortex is generated with high radial velocity gradients originating cavitation.
- implified testcase of a mixer containing a rotor and a stator, providing useful information of the rotor/stator interface performance and accuracy.

The main characteristics observed in all these cases allowed to approach in a more efficient way the final case which is:

- The industrial demonstration case of a passenger ship propeller (P1356).

Special attention was paid during the execution of the project to the two-phase (water-vapour) modelling, the turbulent pressure fluctuation analysis, the influence of non-condensable gases dissolved in the fluid on cavitation (so-called gas cavitation) and the maintainability of flow solution accuracy by splitting the domain into a rotating part and a static part in the case of the industrial test case, i.e. the propeller.

In all cases the simulations have been carried out following the Best Practice Guidelines, applying a hierarchy of refined grids and looking for grid-independent solutions, thereby separating numerical from model errors. The numerical results have been compared to those in literature or those obtained at the experimental facilities by SVA Potsdam, showing a satisfactory agreement in most of the investigated cases.

---

[3] ANSYS CFX is a CFD-Software by ANSYS Inc.

3. Mathematical Model

Equation Section 2

3.1. Cavitation Model

The cavitation model developed for ANSYS CFX is based on the Rayleigh-Plesset equation, which describes the growth of a vapour bubble in a liquid. Thereby the production of vapour due to cavitation is taken into account by adding a special source term into the continuity equation. A homogeneous approximation to the vapour-water flow is adopted, considering the same velocity field for all phases by assuming that the vapour bubbles are moving with the continuous phase without slip velocity.

The governing equations for the two-phase flow then read:

Continuity equation for each phase

$$\frac{\partial(r_\alpha \rho_\alpha)}{\partial t} + \frac{\partial(r_\alpha \rho_\alpha u_i)}{\partial x_i} = \dot{S}_\alpha \tag{2.1}$$

Momentum conservation equation

$$\frac{\partial(\rho_m u_i)}{\partial t} + \frac{\partial(\rho_m u_i u_i)}{\partial x_j} = \frac{\partial P}{\partial x_i} + \rho_m r_\alpha g_i + \frac{\partial(\tau_{ij})}{\partial x_j} \tag{2.2}$$

where r_α, u_i, ρ_α, $\dot{S}_\alpha$, g_i, τ_{ij} and P, are the phase volume fraction, the cartesian velocity components, the phase density, the phase mass generation rate, the acceleration components due to gravity, the pressure and the stress tensor, respectively. Subscript m refers to mixture properties. Since the sum of all phases must occupy the whole domain volume, the following constraint must be satisfied:

$$\sum_{\alpha=1}^{N} r_\alpha = 1 \tag{2.3}$$

where $N = 2$ is the number of phases.
In addition, assuming that the mass sources are due to the interphase mass transfer, it becomes that:

$$\sum_{\alpha=1}^{N} \dot{S}_\alpha = 0 \tag{2.4}$$

When only two phases are involved, as occurs in case of a cavitating flow (vapour and liquid) the mass transfer rates are related by:

$$\dot{S}_v = -\dot{S}_l = \dot{S}_{lv} \tag{2.5}$$

The expression to evaluate this mass source term can be derived from the Rayleigh-Plesset equation, which in its full version can be written as:

$$R_B \frac{d^2R_B}{dt^2} + \frac{3}{2}\left(\frac{dR_B}{dt}\right)^2 + \frac{2\sigma}{\rho_l R_B} = \frac{P_v - P}{\rho_l} \qquad \textbf{(2.6)}$$

where R_B represents the bubble radius, σ is the surface tension coefficient and P_v is the pressure in the bubble, which is assumed to be the vapour pressure. Neglecting the second order terms and the surface tension, the equation reduces to:

$$\frac{dR_B}{dt} = \sqrt{\frac{2}{3}\frac{P_v - P}{\rho_l}} \qquad \textbf{(2.7)}$$

The rate of change of bubble mass is then predicted as:

$$\frac{dm_B}{dt} = \rho_v \frac{dV_B}{dt} = \rho_v 4\pi R_B^2 \sqrt{\frac{2}{3}\frac{P_v - P}{\rho_l}} \qquad \textbf{(2.8)}$$

Assuming that there are N_B bubbles per unit volume, the vapour volume fraction may be expressed as:

$$r_v = V_B N_B = \frac{4}{3}\pi R_B^3 N_B \qquad \textbf{(2.9)}$$

And therefore the total interphase mass transfer due to cavitation per unit volume becomes:

$$\dot{S}_{lv} = \frac{3 r_v \rho_v}{R_B}\sqrt{\frac{2}{3}\frac{P_v - P}{\rho_l}} \qquad \textbf{(2.10)}$$

This expression has been derived assuming bubble growth (evaporation). It can be generalised to include condensation by including an empirical factor (*F*) in the following manner

$$\dot{S}_{lv} = F\frac{3 r_v \rho_v}{R_B}\sqrt{\frac{2}{3}\frac{|P_v - P|}{\rho_l}}\, sign(P_v - P) \qquad \textbf{(2.11)}$$

which may differ for condensation and evaporation, and it is designed to take into account the fact that both processes occur at different rates, since the condensation process is usually much slower than evaporation.

Despite the fact that the model has been generalised for evaporation and condensation, it requires further modification in the case of evaporation. Evaporation is initiated at nucleation sites. As the vapour volume fraction increases, the nucleation site density must decrease accordingly, since there is less liquid. Therefore for evaporation r_v is replaced by $r_{nuc}(1-r_v)$.

The final form of the cavitation model is:

$$\dot{S}_{lv} = \begin{cases} F_{vap} \dfrac{3r_{nuc}(1-r_v)\rho_v}{R_B} \sqrt{\dfrac{2}{3}\dfrac{P_v - P}{\rho_l}} & \text{if } P < P_v \\ F_{cond} \dfrac{3r_v\rho_v}{R_B} \sqrt{\dfrac{2}{3}\dfrac{P_v - P}{\rho_l}} & \text{if } P > P_v \end{cases} \quad \textbf{(2.12)}$$

In this final model formulation the following model parameters have been applied: $R_B = 10^{-6} m,\ r_{nuc} = 5\times10^{-4},\ F_{vap} = 50,\ F_{cond} = 0.01$.

3.1.1. The Turbulent Pressure Fluctuation Model

As discussed before, the influence of the turbulence on the cavitation process has been widely observed in multiple experimental investigations. Turbulent pressure fluctuations can lead to a local decrease in pressure below the vapour pressure and therefore to cavitation. From point of view of maximum accuracy it would be desirable to fully resolve these pressure fluctuations in a CFD simulation, but due to the extreme high numerical effort for Direct Numerical Simulation (DNS) or LES-like turbulence model approaches this is unfortunately not feasible for most technical applications. A different approach to account for enhancement of cavitation due to turbulent pressure fluctuations consists of relating them to the turbulence kinetic energy. In this case, the minimum possible local pressure is represented by the time averaged mean pressure minus the maximum of turbulent pressure fluctuation:

$$P_v - P = P_{sat} - (\overline{P} - P'_{turb}) \quad \textbf{(2.13)}$$

where

$$P'_{turb} = 0.39\rho k \quad \textbf{(2.14)}$$

Thus, the Rayleigh-Plesset equation (2.7) applied for the computation of the cavitation bubble growth becomes:

$$\frac{dR_B}{dt} = \sqrt{\frac{2}{3}\frac{P_{sat} - P + P'_{turb}}{\rho_l}} \quad \textbf{(2.15)}$$

This strategy was found to be not completely physically realistic and therefore a further slight modification was done by the authors in order to make it more rigorous. Since the kinetic energy is related to the turbulence of the liquid phase, water in the current situation, it seemed more appropriate to apply the pressure turbulence term only in its presence. Therefore, the expression (2.14) was changed to:

$$P'_{turb} = 0.39(1 - r_v)\rho k \quad \textbf{(2.16)}$$

which vanishes when the volume is filled up only with vapour, e.g. in larger cavitation bubbles.

3.1.2. The Full Cavitation Model

The formulation presented in the previous section allows modelling the evaporation and condensation phenomena between a liquid phase and its gaseous phase. The models based on the Rayleigh-Plesset equation consider as a driving force of the process the difference between the pressure field and the vapour pressure of the fluid.
Real configurations do not contain pure substances but also an amount of non condensable gases. Their presence affects the onset of cavitation, which can occur in earlier stages (i.e. by higher pressure field values). Therefore, the accurate modelling of such situations represents an important improvement, in order to optimize the design of the ship components.

The modelling of the desorption and absorption phenomena can be also performed [18][19] in an analogous way to the Rayleigh-Plesset equation, it means by solving an extra equation where the driving term is also a pressure difference. In this case the difference between the pressure field and the equilibrium pressure.

The model, as used inside ANSYS CFX, considers a three phase flow configuration, where there is a liquid two-component phase, being the components the original fluid and the dissolved non condensable gas. The other two phases are the vapour of the fluid, and the non condensable gas in its gaseous form. This means, we work with two kinds of “bubbles”.

The mass transfer between the liquid phase and the vapour phase is modelled by means of the Rayleigh-Plesset equation, as described in previous sections. And the mass transfer between the liquid phase and the non condensable gas in its gaseous form is modelled by the Full Cavitation Model, which implies the resolution of one more equation:

$$\frac{\partial}{\partial t}(r_L\rho_W Y_{DA}) + \nabla \bullet ((r_L\rho_W \mathbf{u} Y_{DA}) - \rho_W D_W (\nabla Y_{DA}))) = S_{DA} \qquad \textbf{(2.17)}$$

where Y_{DA} is the mass fraction of dissolved non condensable gas into the liquid phase, and S_{DA} is the source term of the equation. It looks like

$$S_{DA} = R'_{abs} - R'_{des} \qquad \textbf{(2.18)}$$

being R_{abs}' and R_{des}' the mass transfer rate due to absorption and desorption, respectively.

$$R'_{abs} = C_a\rho_A(P - P_{equil})(f_{g,l,\lim} - Y_{DA}\frac{\rho_W r_L}{\rho})\frac{\rho_A r_A}{\rho} \qquad \textbf{(2.19)}$$

$$R'_{des} = C_d\rho_A(P_{equil} - P)(1.0 - \frac{\rho_A r_A}{\rho})Y_{DA}\frac{\rho_W r_L}{\rho} \qquad \textbf{(2.20)}$$

As mentioned before, the driving term now is the difference between the pressure field and the non condensable gas equilibrium pressure. $f_{g,l,\lim}$ represents the maximum solubility of the non condensable gas into the fluid, and it plays the role of limiter of mass transfer rate. C_a and C_d are constants which may be calibrated depending on the type of fluid. For water-air configurations their value is 0.1 and 2.0 respectively.
Accurate values of the equilibrium pressure and maximum solubility must be used to feed the model, which is depending of the kind of fluid (hydraulic oils for instance) not always an easy task. The evaluation of the equilibrium pressure for the present investigations has been carried out by using the Henry’s Law [21]. It computes the equilibrium pressure based on the

mass fraction (or molar fraction) of the non condensable gas present, and a collection of constants for a large amount of different fluids [22]

$$P_G = H_{DA} X_{DA} \tag{2.21}$$

3.1.2.1. Validation

In order to validate the implementation of the Full Cavitation Model performed a test case available in literature [18][19] has been investigated. This is the sudden contraction of a pipe with sharp edges.

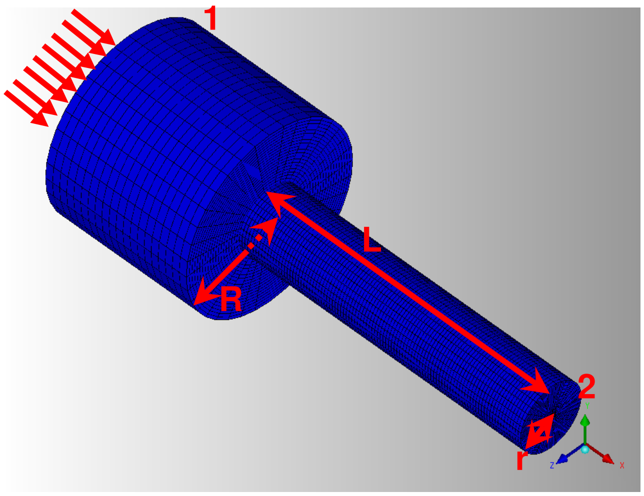

D/d	2.88
L/d	5
P_1	variable
P_2	0.95 bar
r_{A1}	0.124
Y_{DA1}	$1.5x10^{-5}$
Re	$5x10^3:10^4$

Figure 1: Sharp edged orifice geometry and main parameters.

The pressure at the outlet is fixed to 0.95 Bar while the inlet pressure is modified in order to generate different pressure drops (and cavitation numbers). The gaseous air volume fraction at the inlet is equal to 0.124, and the mass fraction of dissolved air into the liquid phase is equal to $1.5x10^{-5}$.

Following Best Practice Guidelines, four different refined grids were used for the investigations (from the coarsest one with 2800 nodes to the fines one with almost 180000 nodes). Details are given in Table 1

Grid	Nodes
1	2800
2	11200
3	44800
4	179200

Table 1: Grid statistics.

The turbulence was modeled by means of the standard k-ε formulation, in order to reproduce the configuration in the literature. For such kind of applications a significant value of the flow is the so-called *Discharge Coefficient*, which measures the ratio between the real mass flow and the ideal one considering the Bernoulli equation and mass conservation.

$$C_d = \frac{\text{mass flow}}{\text{ideal mass flow}} = \frac{\dot{m}}{A_2 \sqrt{2\rho_W (P_1 - P_2) \Big/ \left(1 - \dfrac{A_2^2}{A_1^2}\right)}} \quad \textbf{(2.22)}$$

The numerical discharge coefficient computed with the simulations can be compared to experimental correlations obtained by Nurick [20] for many configurations depending on the shape, Reynolds number, etc. For the current configuration, it takes the following value

$$C_d = 0.62\sqrt{\frac{P_1 - P_V}{P_1 - P_2}} = 0.62\sqrt{\sigma} \quad \textbf{(2.23)}$$

The results of this comparison are summarized in Figure 2. It can be observed a good agreement between the numerical results (points) and the Nurick's correlation (black line) for almost all cavitation numbers. However, for the largest ones, a larger discrepancy appears. This was due to the turbulence modeling. And when it was changed to a SST formulation better results closer to the correlation were obtained.

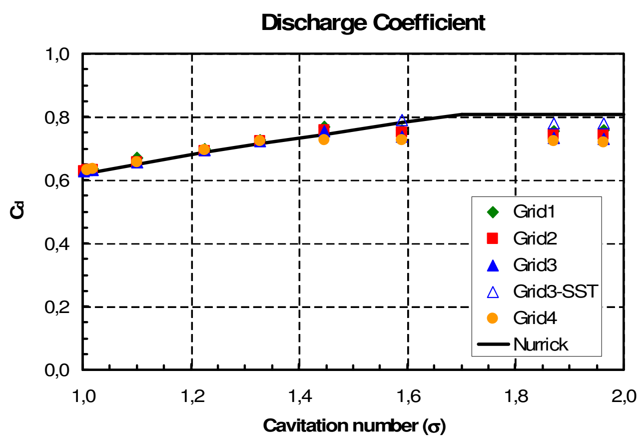

Figure 2: Discharge coefficient *vs*. cavitation number.

As a qualitative result some pictures corresponding to a cavitation number of σ=1.871 are included below. Results to the left correspond to those computed with the Full Cavitation Model and Rayleigh-Plesset Equation Model activated, while results to the right correspond to those computed taking into account only the Raileigh-Plesset Equation Model for cavitation. In Figure 3 (left) it can be seen that just after the contraction some gaseous air is accumulated, not only by effect of the flow (as it occurs in the right picture), but also because of the degassing effect. This can be also appreciated in Figure 4. The amount of dissolved air into the liquid phase is diminished just after the sudden contraction.

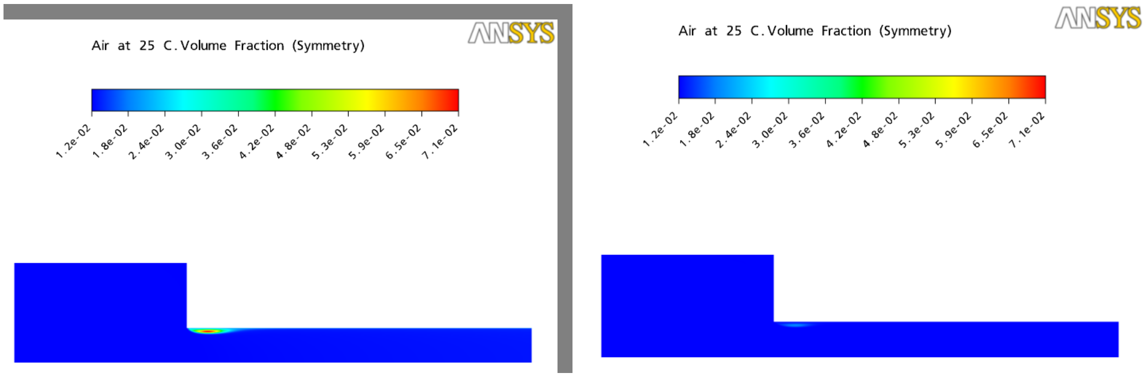

Figure 3: Air volume fraction. σ=1.871. Left:FCM activated. Right: FCM not activated.

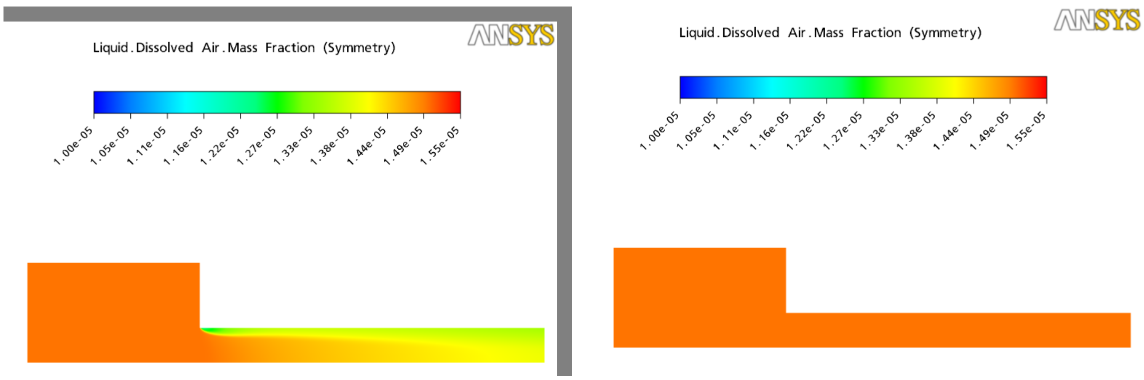

Figure 4: Dissolved Air mass fraction. σ=1.871. Left:FCM activated. Right: FCM not activated.

The results obtained were highly satisfactory, and good agreement with the values in literature was observed.

3.2. Turbulence Modeling

Most of the flows that can be observed in nature or engineering processes are turbulent. It is due to the fact that they are three dimensional flows, unsteady and may contain many different length scales, originating a complex process. The Navier-Stokes equations are still valid for turbulent flows. However, turbulent flows span the range of length and time scales involving scales much smaller than the smallest finite volume size. The computing power required for the Direct Numerical Simulation (DNS) of this kind of flows is further beyond the available one, particularly in cases of industrial interest. Major effort has been carried out by the scientific community in order to take into account the turbulent effects on the flow. Different approaches can be applied such as resolving the large-scale turbulent fluctuations containing the major part of the turbulent kinetic energy (LES, DES, SAS) or modelling the phenomena entirely. When attempting to model the turbulence, turbulence viscosity models can be applied. The turbulence or eddy viscosity models are statistical models and consider that the main variables are compound by an average component and an additional time-varying fluctuating one, like

$$u_i = \overline{u}_i + u_i^{'} \qquad \textbf{(2.24)}$$

Introducing this decomposition into the Navier-Stokes equations (2.1)-(2.2) and time-averaging them, the so-called Reynolds Averaged Navier-Stokes (RANS) equations are obtained

$$\frac{\partial(\rho_m \overline{u}_i)}{\partial t} + \frac{\partial(\rho_m \overline{u}_i \overline{u}_i)}{\partial x_j} = \frac{\partial \overline{P}}{\partial x_i} + \rho_m r_\alpha g_i + \frac{\partial}{\partial x_j}(\overline{\tau}_{ij} - \rho_m \overline{u_i^{'} u_j^{'}}) + S_{M_i} \qquad \textbf{(2.25)}$$

Simulation of RANS equations substantially reduces the computational effort in comparison with DNS and it is generally adopted for engineering applications. However, the averaging procedure introduces additional unknown terms containing products of the fluctuating components, which act like additional stresses in the fluid. These stresses are difficult to determine directly and must be modelled by means of additional equations or quantities in order to close the set of equations. Eddy viscosity models assume that the Reynolds stresses can be related to the mean velocity gradients and turbulent viscosity by the gradient diffusion hypothesis in an analogous manner to Newtonian laminar flow as:

$$\rho_m \overline{u_i^{'} u_j^{'}} = \frac{2}{3}\rho_m k \delta_{ij} + \frac{2}{3}\mu_t \frac{\partial}{\partial x_i}\overline{u}_i \delta_{ij} - \mu_t \left(\frac{\partial}{\partial x_j}\overline{u}_i + \frac{\partial}{\partial x_i}\overline{u}_j \right) \qquad \textbf{(2.26)}$$

where μ_t is the eddy viscosity or turbulent viscosity, and needs to be evaluated. In this work a two-equation turbulence model is applied. It represents a good compromise between numerical effort and computational accuracy. Two extra equations must be solved (k-ε, or k-ω), The turbulent viscosity is modelled as the product of a turbulent velocity and turbulent length scale. The turbulent velocity scale is computed from the turbulent kinetic energy (k), and the turbulent length scale is estimated from either the turbulence kinetic dissipation rate (ε) or the turbulence frequency (ω).

A representative of the two-equation models is the SST (Shear Stress Transport) turbulence model. The SST model [5][23] is based on the combination of two underlying two-equation turbulence models, the industrially wide-spread k-ε -model (Jones and Launder,[26]) , and the k-ω model in the formulation of Wilcox [24][25]. The hybrid procedure consists of the k-equation and a special form of the ω-equation, which enables through changing the value of a blend factor F_1 switching between a ω-equation (F_1=1) and a ε-equation (F_1=0).

The two equations read as:

$$\frac{\partial(\rho_m k)}{\partial t} + \frac{\partial(\rho_m \overline{u}_j k_i)}{\partial x_j} = P_k - \beta^{'} \rho_m k \omega + \frac{\partial}{\partial x_j}\left(\left(\mu + \frac{\mu_t}{\sigma_k} \right) \frac{\partial k}{\partial x_j} \right) \qquad \textbf{(2.27)}$$

and

$$\begin{aligned} \frac{\partial(\rho_m \omega)}{\partial t} + \frac{\partial(\rho_m \overline{u}_j \omega)}{\partial x_j} &= \gamma \frac{1}{\upsilon_t} P_k - \beta \rho_m \omega^2 + \\ &+ \frac{\partial}{\partial x_j}\left(\left(\mu + \frac{\mu_t}{\sigma_k} \right) \frac{\partial \omega}{\partial x_j} \right) + (1 - F_1)\rho_m \frac{2\sigma_{\omega^2}}{\omega} \frac{\partial k}{\partial x_j} \frac{\partial \omega}{\partial x_j} \end{aligned} \qquad \textbf{(2.28)}$$

The value P_k represents the turbulent kinetic energy production term

$$P_k = \min\left[\mu_t\left(\frac{\partial\bar{u}_i}{\partial x_j}+\frac{\partial\bar{u}_j}{\partial x_i}\right)\frac{\partial\bar{u}_i}{\partial x_j}+\frac{2}{3}\rho_m k\delta_{ij}\frac{\partial\bar{u}_i}{\partial x_j},\ 10\cdot\varepsilon\right] \qquad \textbf{(2.29)}$$

while the blending function looks like

$$F_1 = \tanh\left\{\min\left[\max\left(\frac{\sqrt{k}}{\beta^{'}\omega y},\frac{500\upsilon}{y^2\omega}\right),\frac{4\rho_m\sigma_{\omega 2}k}{CD_{k\omega}y^2}\right]^4\right\} \qquad \textbf{(2.30)}$$

being $CD_{k\omega} = \max\left[2\rho_m\sigma_{\omega 2}\frac{1}{\omega}\frac{\partial k}{\partial x_i}\frac{\partial\omega}{\partial x_i},10^{-10}\right]$, and $\beta^{'}=0.0$.

Then the turbulent viscosity can be computed as:

$\mu_t = \rho_m\frac{a_1 k}{\max\left(a_1\omega s F_2\right)}$, with $s=\sqrt{S_{ij}S_{ji}}$, $a_1 = 0.31$ and $F_2 = \tanh\left[\left(\max\left(\frac{2\sqrt{k}}{\beta^{'}\omega y},\frac{500\upsilon}{y^2\omega}\right)\right)\right]$.

In order to become free from effects of the curvature or rotation of the overall system, corrections to the model were introduced. One of them was suggested by Spalart and Shur [27], based on the value s/ϖ (ϖ is the thickness of the eddy). A factor introducing a correction of the turbulence size is included. For the SST model applied, the correction factor f_r (Langtry and Menter [37]) for the production term is computed as

$$f_r = \max\left[\min\left(\frac{(1+c_{r1})2r^*}{1+r^*}\left\{1-c_{r3}\tan^{-1}(c_{r2}\tilde{r})\right\}-c_{r1},1.25\right),0.0\right] \qquad \textbf{(2.31)}$$

where

$r^* = \frac{s}{\sqrt{2\tilde{\omega}_{ij}\tilde{\omega}_{ij}}}$;

$\tilde{r} = \omega_{ij}^{RC}\left(\frac{2\tilde{\omega}_{ik}}{\tilde{\omega}_G}\right)D^{-1/2}$;

$\omega_{ij}^{RC} = S_{jk}\left(\frac{DS_{ij}}{Dt}+\left[\varepsilon_{i\min}S_{jn}+\varepsilon_{j\min}S_{in}\right]\Omega_m\right)D^{-1}$;

$\tilde{\omega}_{ij} = 0.5\cdot\left[\frac{\partial u_i}{\partial x_j}-\frac{\partial u_j}{\partial x_i}\right]+\varepsilon_{mji}\Omega_m$; $\tilde{\omega}_G = \left(\tilde{\omega}_{12}^2+\tilde{\omega}_{13}^2+\tilde{\omega}_{23}^2\right)^{1/2}$;

ε_{mno} is the permutations symbol, Ω_m is the rotation velocity of the system, $D = \max(s^2, c_{r4}, \omega^2)$, c_{r1}=1.0, c_{r2}=2.0, c_{r3}=1.0, c_{r4}=0.09.

When the stress tensor components must be computed more accurately or the underlying assumption of isotropic turbulence is violated, Reynolds Stress Models can be employed. They are based on transport equations for all components of the Reynolds stress tensor and the dissipation rate (or the turbulence frequency). Algebraic Reynolds Stress models solve algebraic equations for each individual component of the tensor, while differential methods solve a differential transport equation. In this case the computational effort is consequently increased. An ω-based Reynolds Stress model was chosen for the present work: the so-called BSL Reynolds stress model. In this case the modelled equations for the Reynolds stresses can be written as follows:

$$\frac{\partial(\rho\tau_{ij})}{\partial t}+\frac{\partial(\overline{u}_k\rho\tau_{ij})}{\partial x_k}=-\rho P_{ij}+\frac{2}{3}\beta^{'}\rho\omega k\delta_{ij}-\rho\Pi_{ij}+\frac{\partial}{\partial x_k}\left(\left(\mu+\frac{\mu_t}{\sigma^*}\right)\frac{\partial\tau_{ij}}{\partial x_k}\right) \qquad \textbf{(2.32)}$$

And the corresponding ω-equation read as:

$$\begin{aligned}\frac{\partial(\rho\omega)}{\partial t}+\frac{\partial(\overline{u}_k\rho\omega)}{\partial x_k} &= \alpha_3\frac{\omega}{k}P_k-\beta_3\rho\omega^2+\\ &+\frac{\partial}{\partial x_k}\left[\left(\mu+\frac{\mu_t}{\sigma_{\omega3}}\right)\frac{\partial\omega}{\partial x_k}\right]+(1-F_1)2\rho\frac{1}{\sigma_2\omega}\frac{\partial k}{\partial x_k}\frac{\partial\omega}{\partial x_k}\end{aligned} \qquad \textbf{(2.33)}$$

Again the model blends from a ω-based model to an ε-based model. In the first case, the following parameters are employed, $\sigma_1^*=2.0$, $\sigma_1=2.0$, $\beta_1=0.075$, $\alpha_1=0.553$ while in the second case, they are $\sigma_2^*=1.0$, $\sigma_2=0.856$, $\beta_2=0.0828$, $\alpha_2=0.44$.The blending is done by means of a smooth linear interpolation in a similar way as for the SST method [13].
The constitutive pressure-strain correlation is given by

$$\Pi_{ij}=\beta^{'}C_1\omega\left(\tau_{ij}+\frac{2}{3}k\delta_{ij}\right)-\hat{\alpha}\left(P_{ij}-\frac{2}{3}P\delta_{ij}\right)-\hat{\beta}\left(D_{ij}-\frac{2}{3}P\delta_{ij}\right)-\hat{\gamma}k\left(S_{ij}-\frac{1}{3}S_{kk}\delta_{ij}\right) \qquad \textbf{(2.34)}$$

where the production tensor P_{ij} is computed as

$$P_{ij}=\tau_{ik}\frac{\partial\overline{u}_j}{\partial x_k}+\tau_{jk}\frac{\partial\overline{u}_i}{\partial x_k};P=\frac{1}{2}P_{kk} \qquad \textbf{(2.35)}$$

and the tensor D_{ij} as

$$D_{ij}=\tau_{ik}\frac{\partial\overline{u}_k}{\partial x_j}+\tau_{jk}\frac{\partial\overline{u}_k}{\partial x_i} \qquad \textbf{(2.36)}$$

Finally the turbulent viscosity can be computed as

$$\mu_t=\rho\frac{k}{\omega} \qquad \textbf{(2.37)}$$

The values of the coefficients applied by ANSYS CFX for the computation of this model are:
$\beta'=0.09$, $\hat{\alpha}=(8+C_2)/11$, $\hat{\beta}=(8C_2-2)/11$, $\hat{\gamma}=(60C_2-4)/55$, $C_1=1.8$, $C_2=0.52$
In addition to the turbulence viscosity models, another family of methods can be used known as LES, consisting of filtering the Navier-Stokes equations and the decomposition of the flow variables into a large scale and a small scale. However, this technique is computationally very expensive when it is applied to industrial problems. In this context arises the need of the use of Scale-Adaptive Simulations (SAS). It is an improved URANS formulation, which allows

the resolution of the turbulent spectrum in unstable flow conditions. The SAS method [15] is based on the Von Karman length scale. Depending on it, the model adjusts to a URANS simulation, with LES-like behaviour in unsteady regions, or to RANS simulation in stable flow regions.
As it will be shown in next section, it was found that the use of either a scheme or another plays an important role in the simulation. The Reynolds Stress Model applied (BSL RSM) leaded to more accurate predictions of the rotational velocity (which presents a steep profile) in case of tip vortex cavitation than SST computations.

3.3. Rotor-Stator Interface

In many turbo-machinery applications is the geometry composed by many parts, some of which are static while others move or rotate. In such configurations ANSYS CFX allows to split the domain into rotor and stator subdomains, which are solved every coefficient loop in a time step independently and after every one of them some information from the other side of the interface is transferred in order to reach the proper solution.

This procedure is performed by defining a surface of connection, rotor-stator interface, through which fluxes values are discretized and transferred. The treatment is fully implicit in order not to affect the solution convergence. Fluxes discretized at the interface are: advection, diffusion, pressure in momentum and local pressure gradient.

The fluxes which are discretized at the interface are:
• Advection: Mass out is connected to the upstream values, and mass in is connected to upstream values.
• Diffusion: A diffusion gradient is estimated using the regular shape function based gradient coefficients, but all dependence of the gradient estimate on nodes on the interface are changed to a dependence on interface variables.
• Pressure in momentum: Evaluated using local nodal and control surface pressures and shape function interpolations.
• Local pressure gradient in mass re-distribution: This gradient is estimated using the regular shape function based gradient coefficients, but all dependence of the gradient estimate on nodal pressure on the interface is in terms of the interface pressure variable.

When the grids at both sides of the interface do not match exactly, it is necessary to compute a weight factor to be applied to the computation of the fluxes. This factor is based on the fraction of area of each cell from one side o f the interface in relation with the cells on the other side of the interface.

For configurations like the industrial test case that we are investigating, this is a proper strategy. Only the propeller is rotating while the cavitation tunnel remains fix. A suitable split of the domain in such a case is shown in Figure 5. A cylinder-like surface containing the propeller and the hub is considered as the rotor/stator interface. Through this interface the flux information will be computed and exchanged.

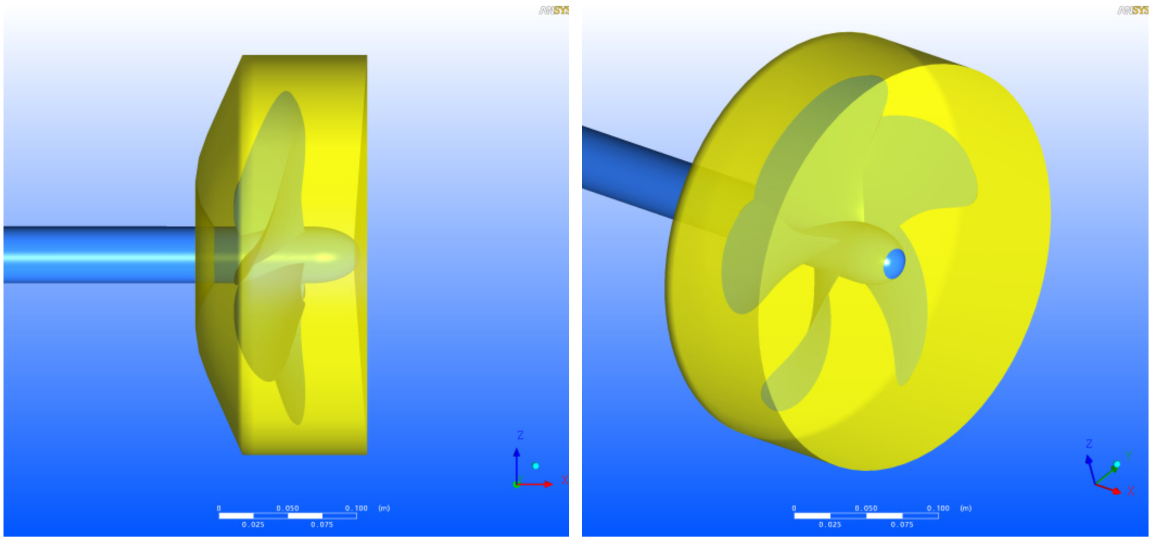

Figure 5: Propeller P1356. View of the rotor/stator domain decomposition. Left: Lateral view; Right: Front view.

3.3.1. Issues & Improvements

As it will be intensively described in the following section, one of the parameters analyzed in the numerical resolution of the flow in the cavitation tunnel with the propellers, is the transient pressure signal at different locations. This was done in order to compare numerical values with the experimental investigations.

It was observed that for some grid configurations at the rotor/stator interface, some non-physical wiggles appear at the profiles. Since the industrial case is very large, a simpler case with similar configuration was chosen to isolate the origin of this behaviour.

The simpler case consists of a two dimensional mixer, where four blades rotate at its center. The geometry of the case is shown in Figure 6.

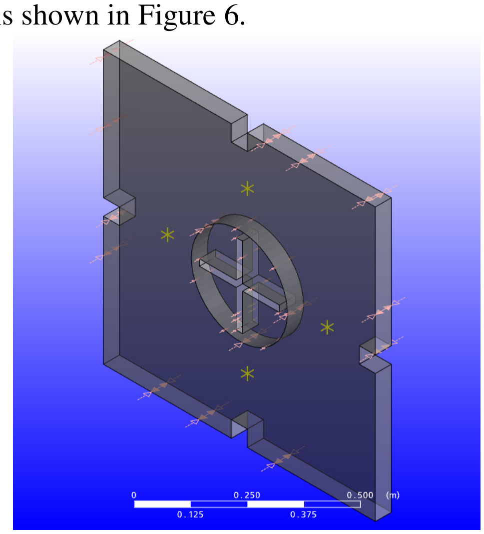

Figure 6: 2D mixer geometry.

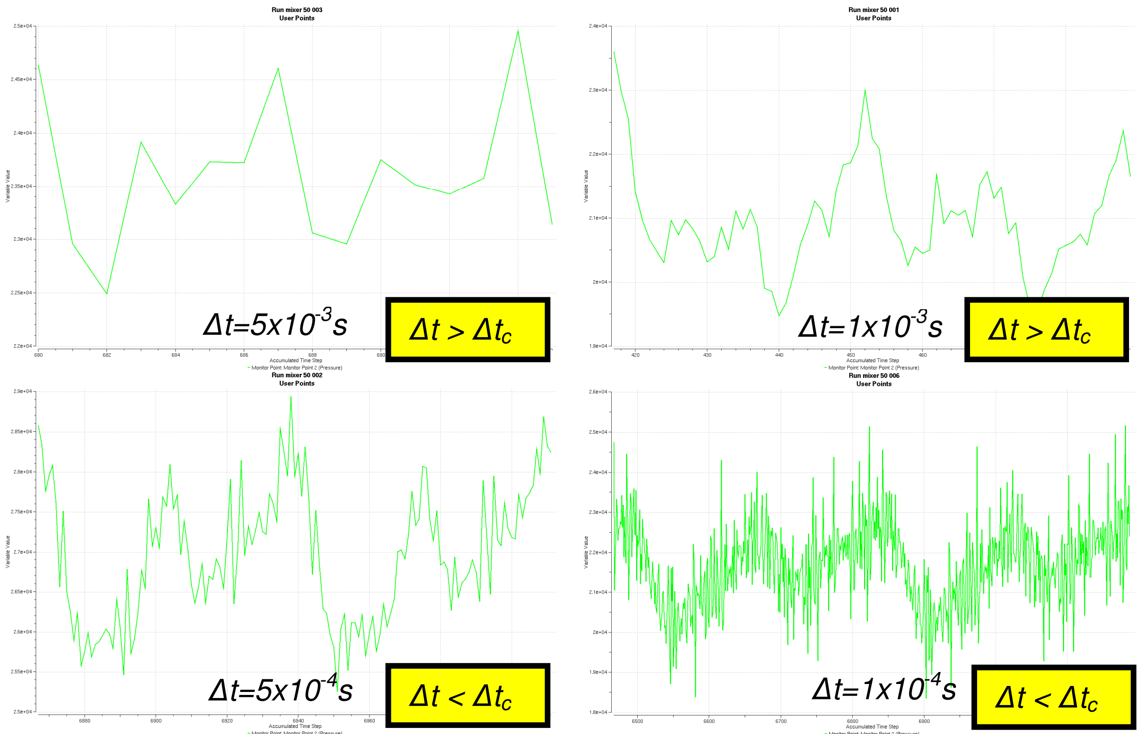

Figure 7: 2D mixer. Transient pressure signal for different time steps.

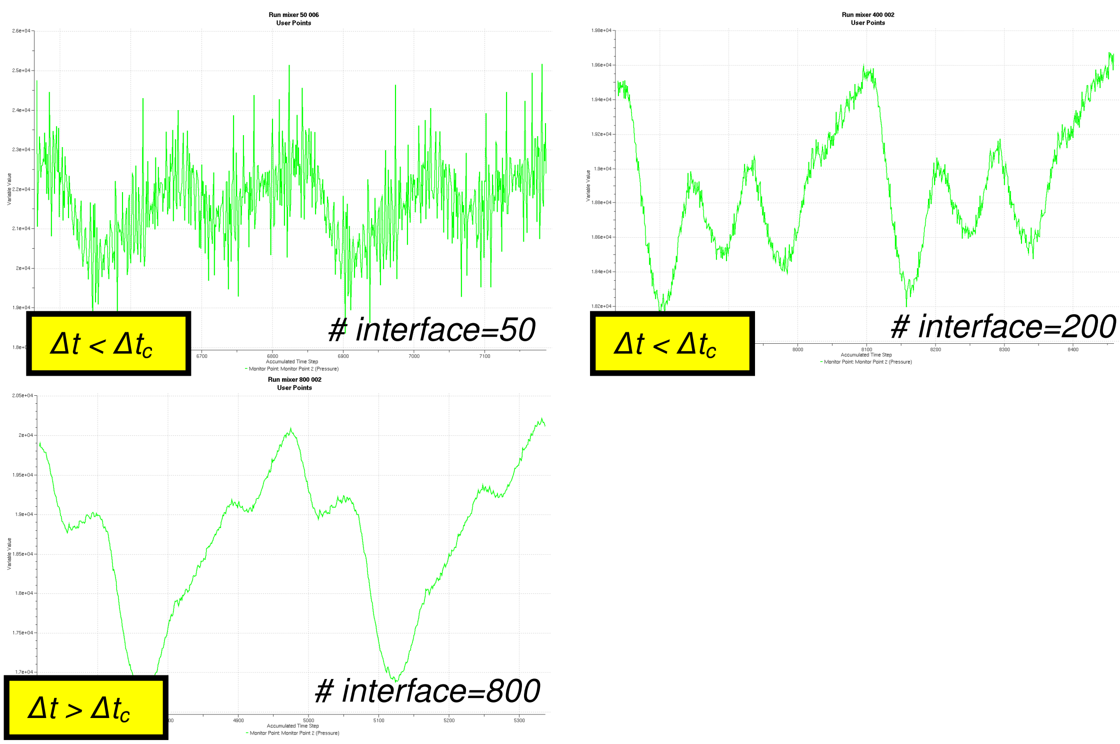

Figure 8: 2D mixer. Transient pressure signal for different grid resolution at the interface.

Series of different simulations were carried out by changing the grid refinement and the time step. A critical time step could be identified, depending on the rotation frequency and the grid resolution.

Assuming a regular discretization at the rotor/stator interface, the critical time step corresponds to jump exactly one cell each time step. This means

$$\Delta t_c[s] * n[s^{-1}] * 2\pi[rad] = 2\pi[rad] / \# cells \tag{2.38}$$

$$\Delta t_c[s] = 1/(\# cells * n[s^{-1}]) \tag{2.39}$$

When $\Delta t < \Delta t_c$, the wiggles pop in (Figure 7and Figure 8). And this was due to the process on the flux evaluation. By improving this procedure we were able to rid off the undesired oscillations on the transient pressure profiles (Figure 9).

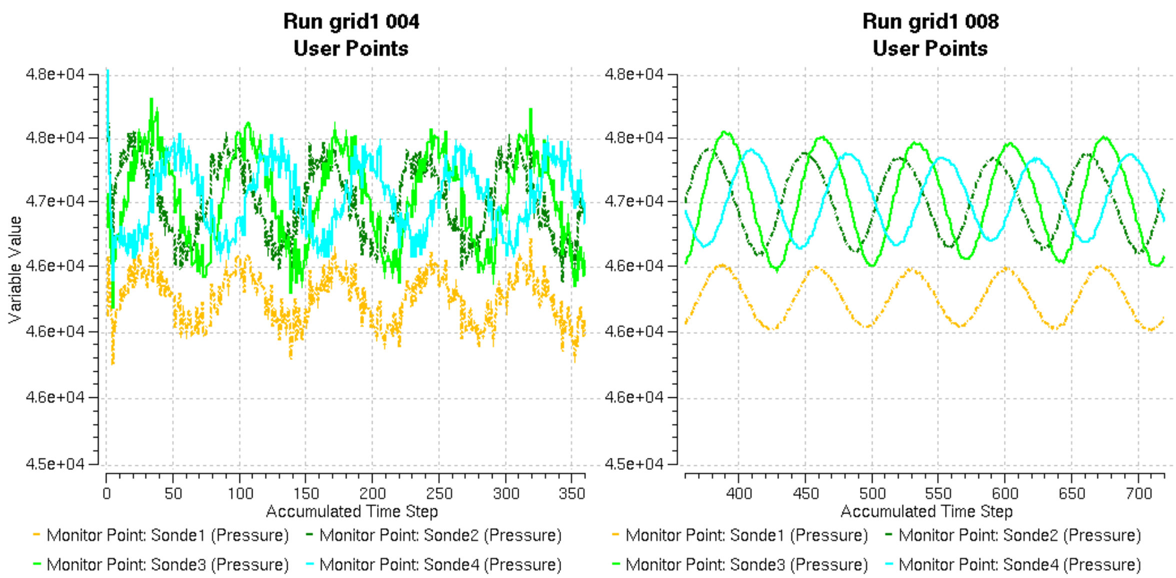

Figure 9: Propeller P1356. Transient pressure signal.

4. Validation Test Cases. Comparison with experimental data.

Equation Section 3

The final goal of this work is to get a deeper understanding of the structure of the flow around a propeller of a passenger ship. The accurate prediction of cavitation has been found out to be intrinsically related to the accurate resolution of turbulent structures of the flow. Therefore, a thoroughly analysis of the turbulence modeling in this kind of application was performed.

Three different cases have been analyzed. The first one is a two dimensional configuration containing a plano-convex profile, where transient cloud cavitation can be observed. The second one is a three dimensional case, where the fluid flows around a NACA 66_2-415 hydrofoil. A tip vortex is generated with high radial velocity gradients originating cavitation. These testcases represent some simplification with respect to the P1356 propeller flow due to the simpler shape of the hydrofoil and the stationary hydrofoil geometry in contrary to the ship propeller rotation. Therefore it can be regarded as an appropriate first approach to the study of the flow around the propeller and formation of turbulence/vortex induced cavitation. The last case is the flow around the P1356 propeller itself. In all cases the simulations have been carried out following the Best Practice Guidelines (BPG) [6], and different grids and turbulence models have been investigated. The numerical results obtained have been compared to the experimental data available in literature for the first and second case, and to experimental data generated at SVA Potsdam, which includes transient pressure signals as well as cavitation patterns, for the propeller case. A highly satisfactory agreement between numerical solutions and experiments is observed for all test cases, showing the appropriateness of the code and models employed in order to solve marine applications.

4.1. Le Profile

4.1.1. Problem definition

A schematic of the experimental setup [2] of Le is given in Figure 1. For the original experiment the hydrofoil was at a submersion depth of 20 cm under a free surface. Its upper side is plane and its lower side circular (radius 26 cm) with a maximum thickness of 20mm. The leading edge is rounded with a radius of 1 mm, so that the chord (c_0) is about 196 mm (Figure 10). Experiments involving different angles of attack (from -8° to 8°), different cavitation numbers and different Reynolds numbers (from 10^6 to $2x10^6$, which correspond to inlet velocities from 5 m/s to 10 m/s) were performed as reported in the original publication by Le [2].

The cavitation number (σ) mainly characterising the flow pattern is defined as:

$$\sigma = \frac{P - P_v}{0.5 \rho v_{in}^2} \qquad \textbf{(3.1)}$$

Configurations within the range of values described by Le were chosen to run the numerical computations, and validate the model in ANSYS CFX.

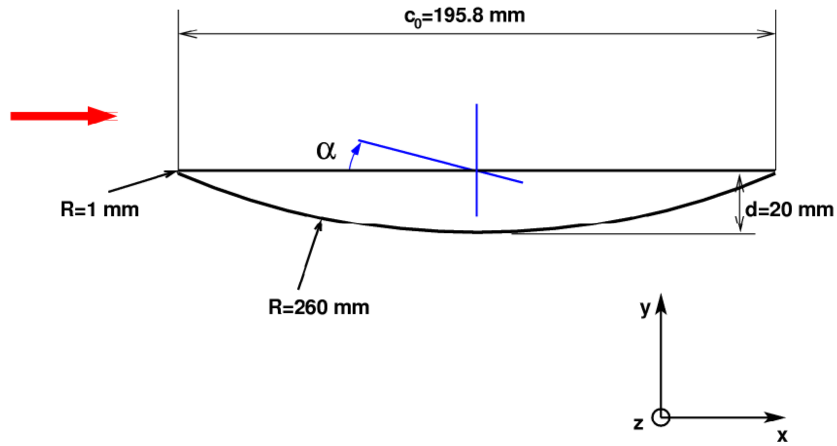

Figure 10: Schematic representation of the flow around a plano-convex hydrofoil.

The configuration chosen to run the CFD simulations is presented in Figure 11. In difference to the original experimental setup the hydrofoil was submerged in a wall bounded channel, thereby avoiding the prediction of the free surface.

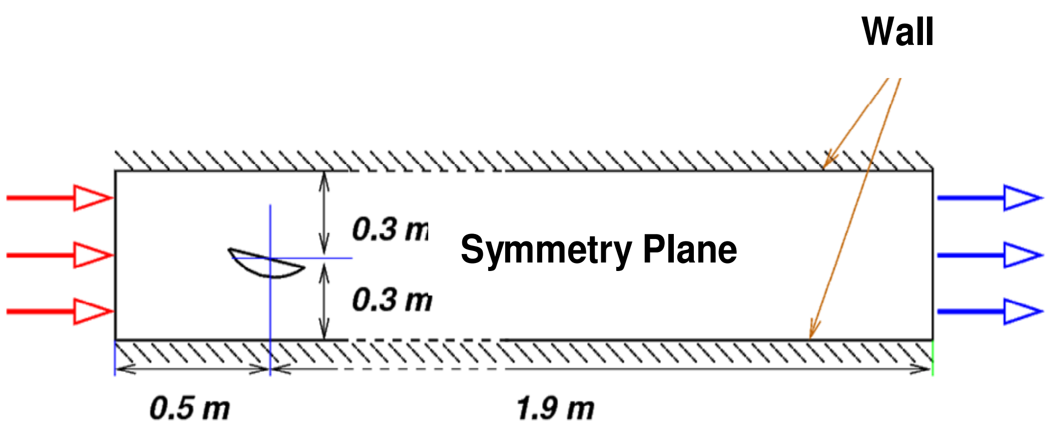

Figure 11: Representation of the setup used for the CFD computations of the Le profile case.

4.1.2. Boundary/Initial conditions

The following boundary conditions were applied to solve the test case:

- Inlet boundary condition with an inlet velocity value based on the Reynolds number.

$$v_{in} = \frac{\mathrm{Re}\,\mu}{\rho L} \quad \textbf{(3.2)}$$

- Outlet boundary condition with a static outlet pressure based on the cavitation number, vapour pressure and velocity at the far field (in this case assumed to be equal to the inlet velocity).

$$p_{out} = p_v + \sigma_n \left(\frac{\rho}{2} v_{in}^2 \right) \quad \textbf{(3.3)}$$

- No-slip wall boundary condition for the cavitation tunnel walls and the solids inside the domain. The CFX automated wall treatment has been applied for turbulence boundary conditions in dependency on y^+ values of the first mesh cell.

4.1.3. Numerical meshes

The discretization of the domain has been performed by means of ICEM CFD Hexa [33] as a grid generator. The blocking structure shown in Figure 3 has been designed to generate the grids. In this manner a smooth and high quality mesh can be obtained (in terms of grid lines angle and aspect ratio). In order to apply the Best Practice Guidelines, the simulations were computed on refined grids. Three levels of refinement are performed obtaining finer meshes, since the quality of the mesh can determine significantly the accuracy of the simulation executed on it.
The refinement factor is 2 in each coordinate direction, while the minimum grid angle value is around 40° for all three cases. An important attribute of the mesh to take into account is the distance of the first node of the grid to the wall, particularly when turbulence models are applied. For all three meshes this value is small enough to expect a satisfactory resolution of the turbulent boundary layer near the wall. It can be computed as

$$\Delta y = L\sqrt{80}\,\mathrm{Re}_L^{-13/14}\,\Delta y^+ \quad \textbf{(3.4)}$$

Grid	**Coarse**	**Medium**	**Fine**
# nodes	56,452	224,264	893,986
# elements	27,840	111,360	445,440
Minimum grid angle	41	38	43
First layer distance y [µm]	10	5	2.5
Average y^+	4	2	1

Table 2: Grid statistics for the Le profile test case.

The grid has been changed not only by refinement but also by rotating the angle of attack of the flow against the hydrofoil in order to deal with different configurations. In this case, the same blocking structure can be employed, and by rotating the blocks adjacent to the hydrofoil, the grids can be updated to the current angle.

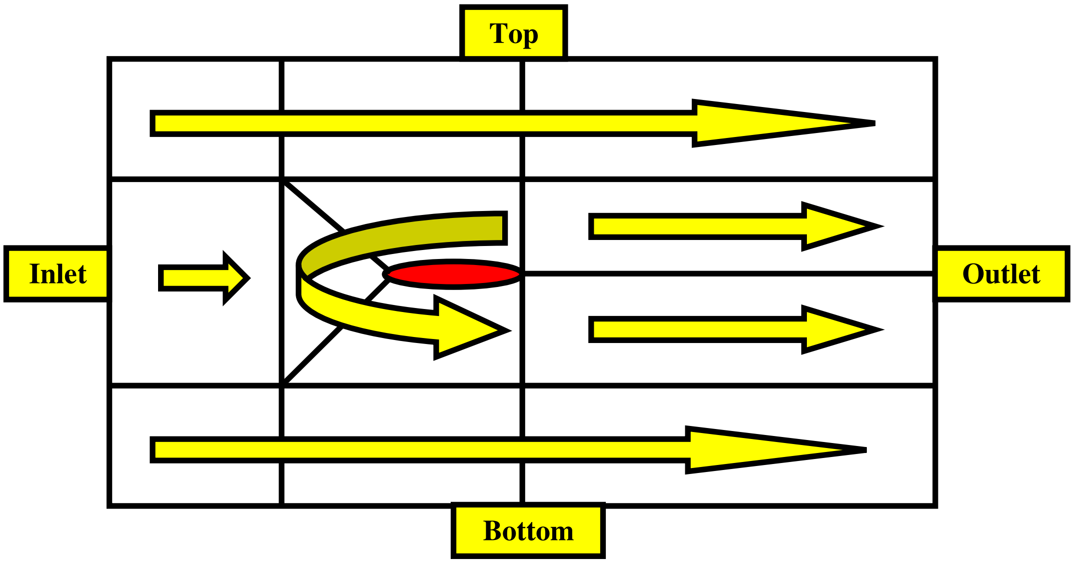

Figure 12: Blocking structure.

The main characteristics of the grids created for the numerical simulations are summarized in Table 2, and a representation of one of the coarse meshes involved in the calculations is shown in Figure 13.

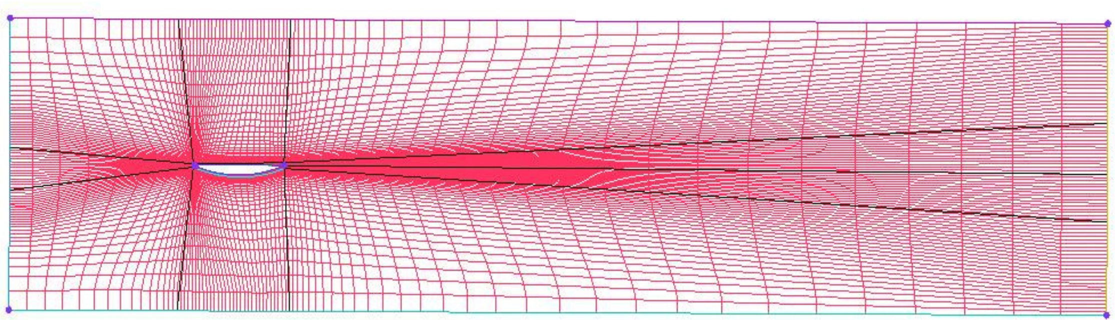

Figure 13: Coarse mesh.

4.1.4. Computation strategy

Once the meshes were generated, steady state simulations were carried out. However, some configurations appeared to be transient, specifically those with lower cavitation number or larger angle of attack. In these cases the cavitation bubbles become oscillatory or are even partially removed from the hydrofoil surface by the incident fluid flow. Thus, transient simulations had to be carried out for these configurations. The ANSYS CFX setup then must be updated introducing an arithmetical averaging procedure to be applied to the main flow variables, which originates an average pressure, average velocity and average volume fraction field to be compared to the experimental data.

4.1.5. Results

4.1.5.1. Cavitation prediction

The described oscillatory flow behavior can be observed in Figure 14, where a whole transient cycle is shown for a configuration of α=4°, and σ=0.5.

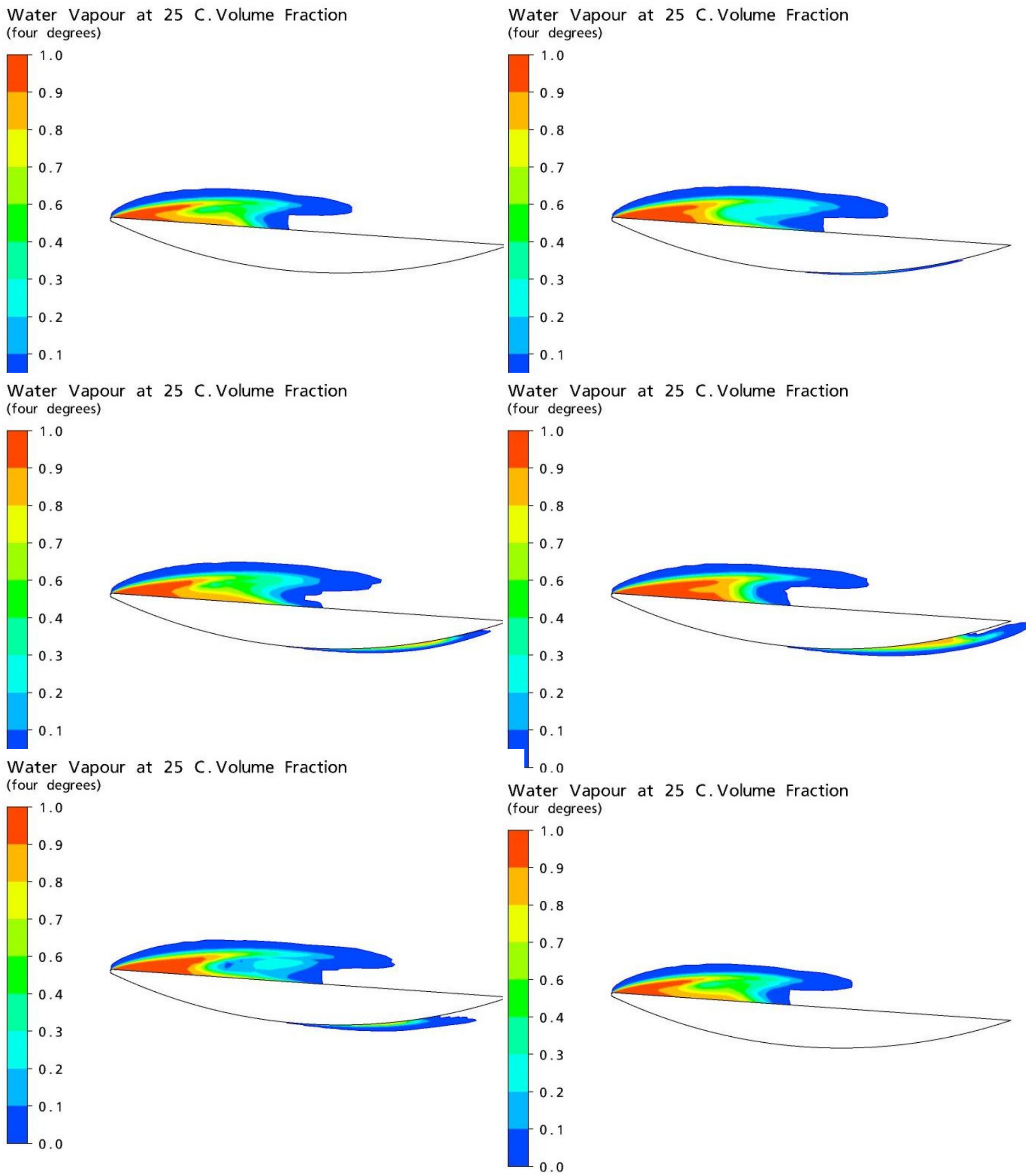

Figure 14; Transient cycle of an oscillating cavitation region on upper side of the hydrofoil for α=4°, and σ=0.5.

In order to examine cavitation for the different configurations the length of the cavitation zone attached to the upper side of the hydrofoil is measured. An investigation of the influence of both the cavitation number and the angle of attack was performed. It is observed in Figure 15 [4] that the larger the cavitation number is, the lower cavitation length is obtained. In addition, the impact of the angle of attack can be seen. The larger the angle of attack is, the larger becomes the cavitation zone and its length.

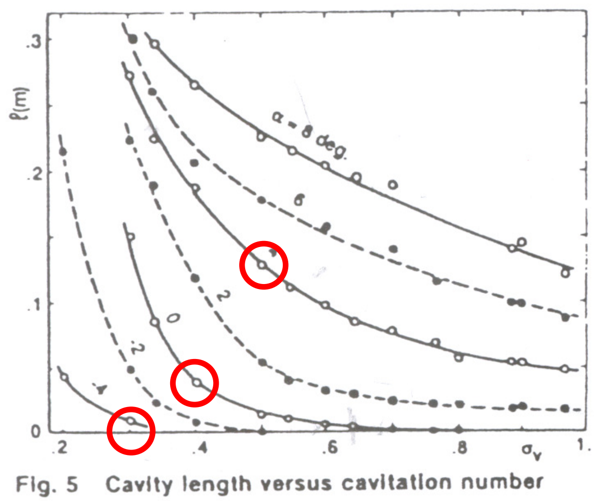

Figure 15: Cavitation length *vs.* cavitation number for different angles of attack.

Three representative results of the computed series out of test case conditions are shown in Figure 16, Figure 17, and Figure 18 corresponding to the vapor volume fraction for an angle of attack of α=0° at a cavitation number of σ=0.4, α=4° with σ=0.5, and α=-4° with σ=0.3 respectively. For the first case, small cavitating areas appear on both upper and lower side, while for the second case only one larger cavitation bubble appears to be attached to the upper side of the hydrofoil. For the third case no cavitation is predicted on the upper side o f the hydrofoil.

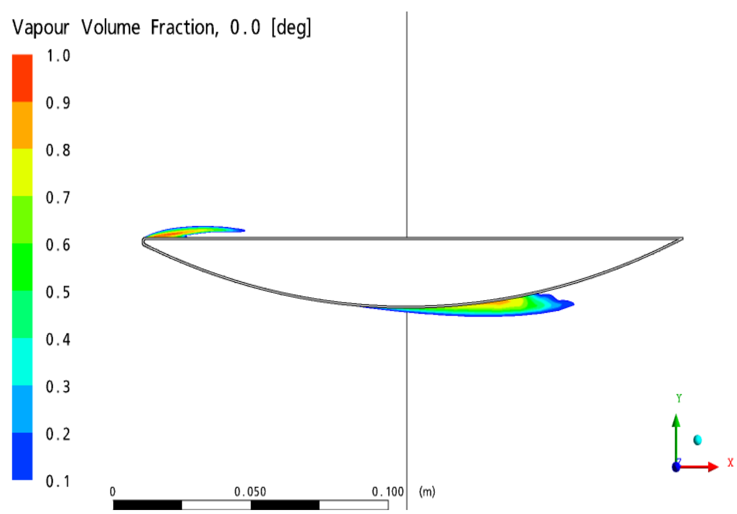

Figure 16: Vapor volume fraction. α=0°, σ=0.4.

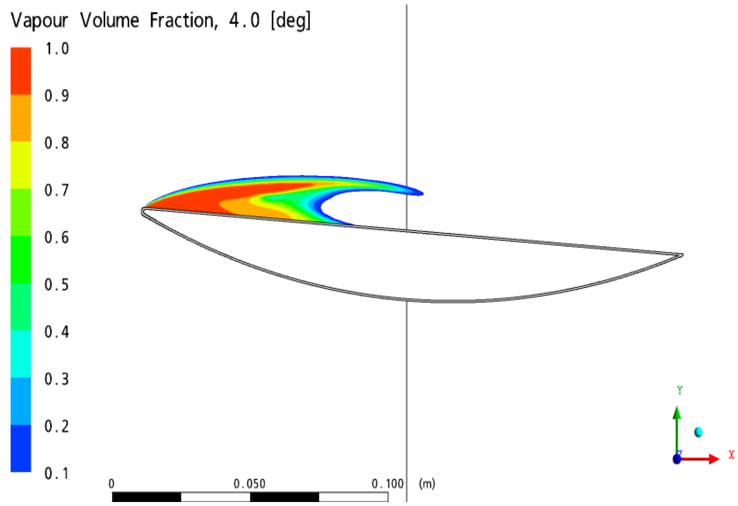

Figure 17: Vapor volume fraction. α=4°, σ=0.5.

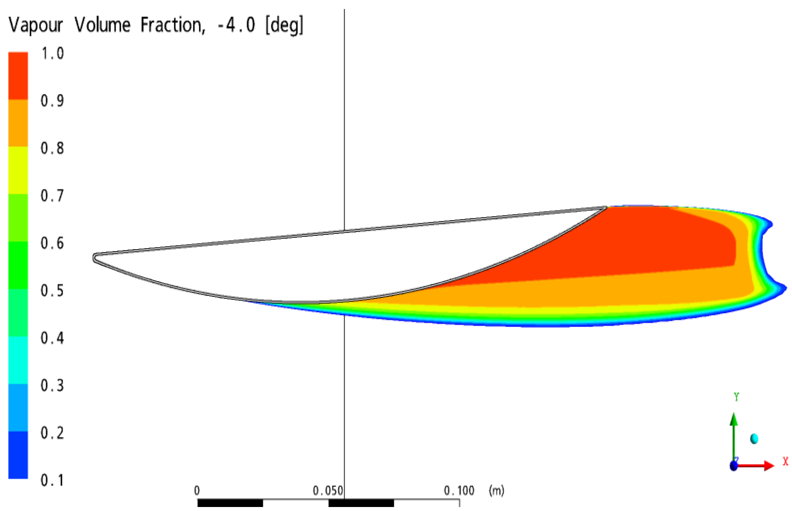

Figure 18: Vapor volume fraction. α=-4°, σ=0.3.

4.1.5.2. Pressure coefficient

The cavitation arises when the pressure drops below the saturation pressure. This can be detected not only by the vapour volume fraction field but also by analyzing the pressure values and comparing to direct pressure measurements at specific locations on the hydrofoil surface. A pressure coefficient can be defined as

$$c_p = \frac{2 \cdot p_{stat}}{\rho_l u_\infty^2} \qquad \textbf{(3.5)}$$

In Figure 19 to Figure 22**,** the pressure coefficient obtained with medium grid simulations is plotted against the experimental results. They correspond to different angles of attack (α=2.5°, 3.5°, 4.1° and 5.1° respectively), while the cavitation number is 0.55 for the first two cases and 0.81 for Figures 11 and 12. At the zone where the pressure coefficient is lower than the cavitation number, evaporation is occurring. It can be noticed by comparing Figure 19 and Figure 20 that the length of the vapour bubble attached to the upper side of the hydrofoil is larger for the case of α=3.5° as expected. The same effect can be seen in Figure 21 and Figure 22. Nevertheless both predicted cavitation bubble lengths are shorter since the cavitation number is larger. Comparing the different curves to the experimental values reasonable agreement in shape is observed, specifically for the first three configurations while for the larger angle of attack at α=5.1° discrepancies appear.

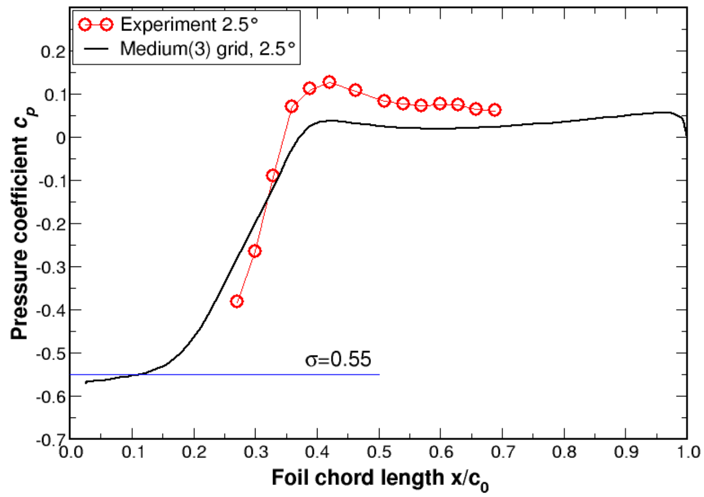

Figure 19: Pressure coefficient, α=2.5°, σ=0.55.

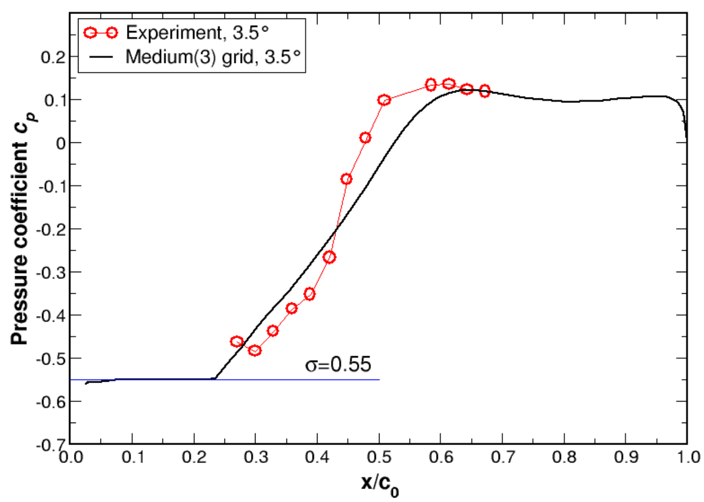

Figure 20: Pressure coefficient, α=3.5°, σ=0.55.

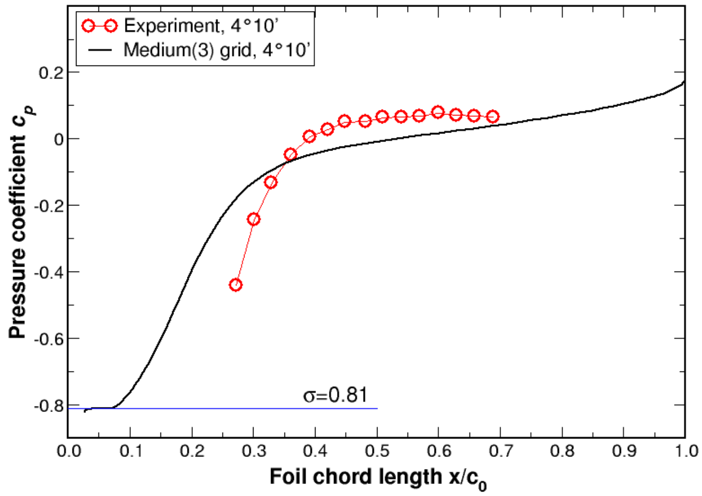

Figure 21: Pressure coefficient, α=4.1°, σ=0.81.

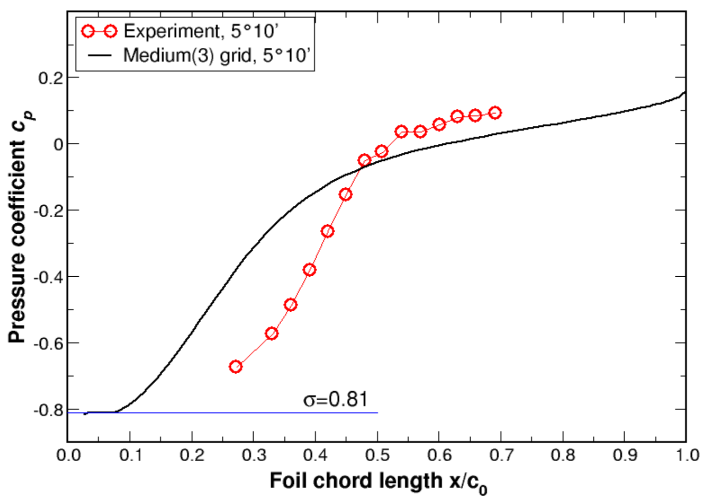

Figure 22: Pressure coefficient, α=5.1°, σ=0.81.

Pressure coefficient can be further used to evaluate the influence of turbulent pressure fluctuations on cavitation in accordance with equation (2.14) and (2.15). In Figure 23 the c_p curves for three different modelling approaches can be compared. The diagram shows results from a simulation using the original Rayleigh Plesset equation, a simulation using the modification to the Rayleigh-Plesset equation described in equation (2.14), and finally a simulation using the modification to the Rayleigh-Plesset equation described in equation (2.16). As mentioned in section 3.1.1, the last expression leads to more realistic results, also observable differences are not very pronounced for this particular test case.

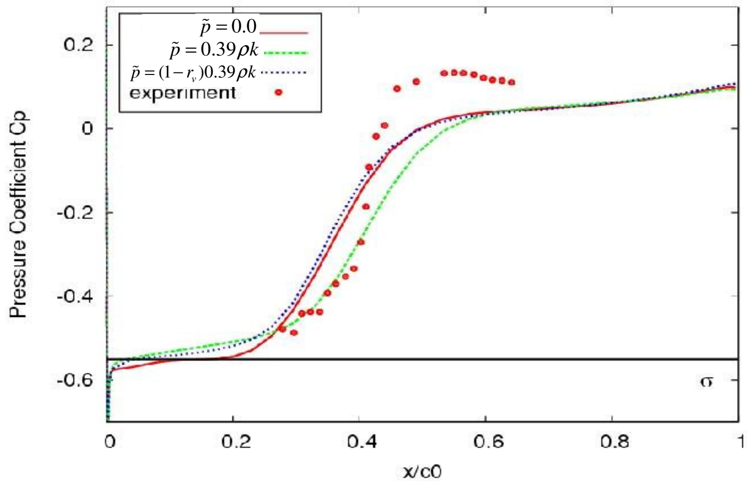

Figure 23: Pressure coefficient in dependency on the modeling approach for the turbulent pressure fluctuation term. α=3.5°, σ=0.55.

4.1.5.3. Lift coefficient

Global values for the different configurations were also investigated and compared to data. This is the case for the lift coefficient, defined as:

$$c_L = \frac{2 \cdot F_L}{\rho_l \cdot u_\infty^2 \cdot A_{blade}} \quad \textbf{(3.6)}$$

where F_L is the lift force, A_{blade} is the area of the hydrofoil and u_∞ is the velocity far upstream the hydrofoil. Figure 24 shows the value of the lift coefficient for different angles of attack as well as for different cavitation numbers. Under non-cavitating conditions the relationship between lift and angle of attack is almost linear, however this behavior is substantially modified when the cavitation number is decreased and cavitation appears.

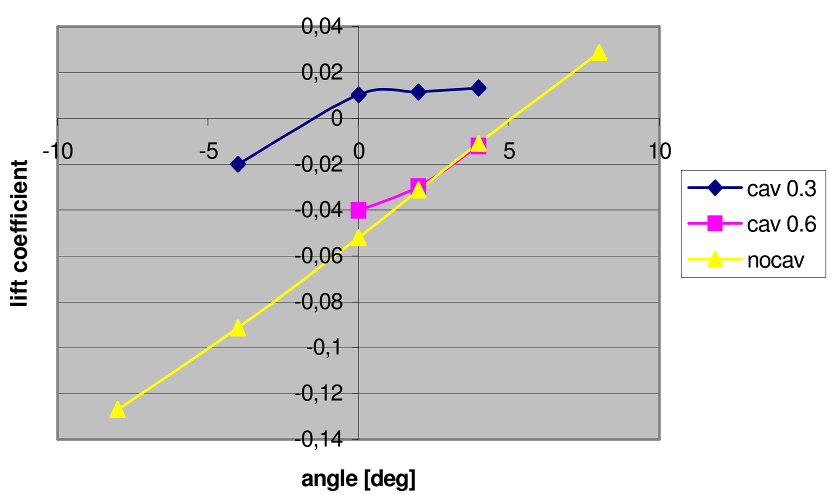

Figure 24: Lift coefficient *vs.* angle of attack for different cavitation number.

4.1.5.4. Influence of the use of Full Cavitation Model (FCM)

If we examine the results in Figure 16, Figure 17, and Figure 18 again, and we compare the cavitation length predicted with the experimental one reproduced in Figure 15, we can observe that this length is under predicted. For the α=0°- σ=0.4 case, the experimental length value is around 20%, which is significantly larger as predicted. For the α=4°- σ=0.5 configuration, the numerical result is around 40% against the 60% in the experiments. The same behavior is observed in the third configuration, α=-4°- σ=0.3, where no cavitation is observed in the numerical solution on the upper side of the hydrofoil, while around a 5% was expected.

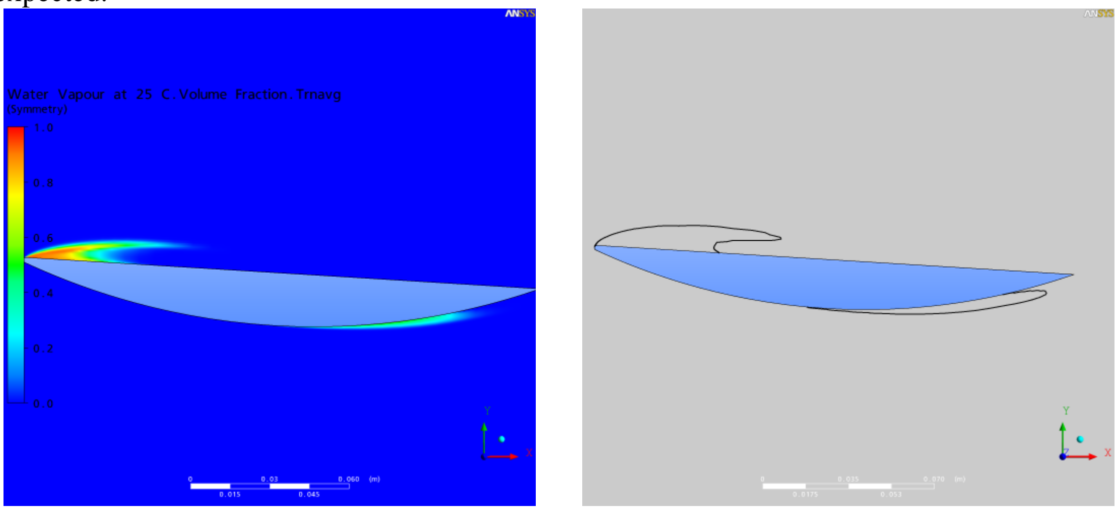

Figure 25: Vapor volume fraction. α=3.2°, σ=0.55.

The case was investigated once more, now taking into account the presence of non-condensable gas, by applying the Full Cavitation Model described before. The configuration corresponds to an angle of attack of α=3.2° and a cavitation number of σ=0.5. The three phases considered in these investigations were liquid (with water and dissolved air), vapor, and gaseous air. The experimental studies for this case point out that the cavitation length on the upper side of the hydrofoil should be around 40% of the chord length.

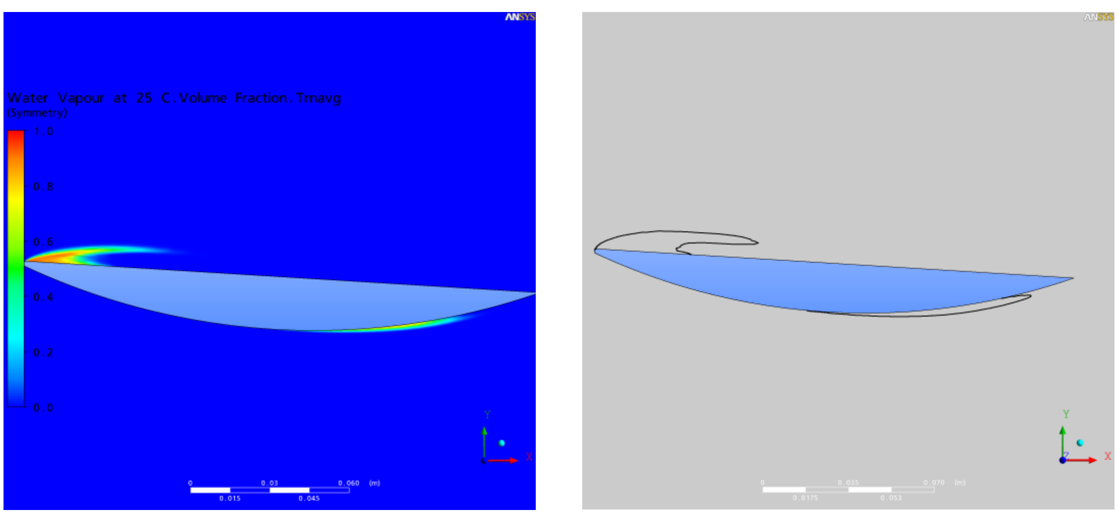

Figure 26: Vapor volume fraction. α=3.2°, σ=0.55, FCM activated

First, the case was simulated considering only water and vapor in the flow. The vapor volume fraction predicted is shown in Figure 25. As for the previous cases, the cavitation length is much shorter as expected (around 20%).

Then, the full cavitation model was activated, and a three phase flow was simulated. The vapor volume fraction is presented in Figure 26. The zone where cavitation is predicted on the upper side of the hydrofoil is even reduced. However, if we move to Figure 27, we will see that some gaseous air is predicted. If we take into account that for the experimental investigations, it is not possible to distinguish between vapor and air, and we "add" the zones where vapor and air appear, we will end up with the profile in Figure 28, which indicates that the vapour and gas cavitation length occurring at the upper side of the hydrofoil is around 40%, as was found in the experiments.

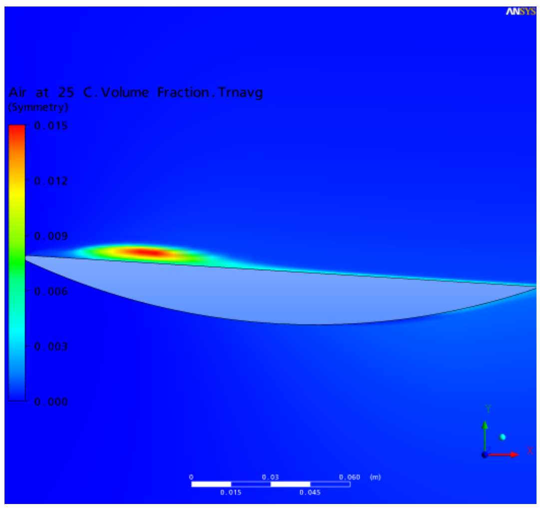

Figure 27: Air volume fraction. α=3.2°, σ=0.55, FCM activated

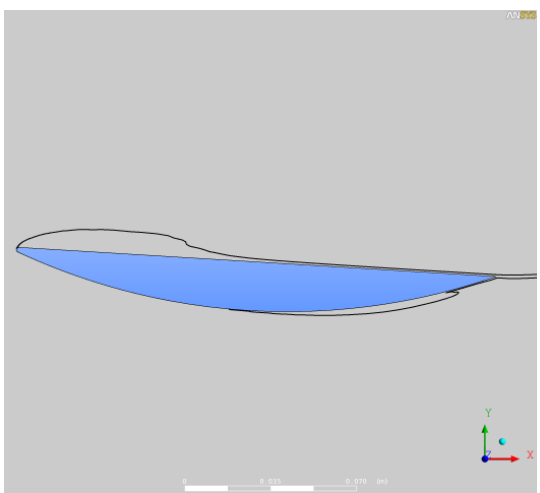

Figure 28: Vapor and air volume fraction border. α=3.2°, σ=0.55, FCM activated

4.1.6. Discussion

A validation of the cavitation model has been performed analyzing a test case well-known in literature and comparing results of the CFD simulations obtained with ANSYS CFX to experimental data.
The test case is based on the experiments made by [2]. In this test case the flow passes around a plano-convex hydrofoil, and cavitation clouds on both sides can be observed. Three refined grids have been used for the simulation, ensuring comparable mesh quality on all grid levels. The cavitation lengths, pressure coefficients and lift values have been investigated and compared against the literature values. The numerical results agree reasonably well to the experiments, even the necessity to use even finer grids could be shown from the present validation study.

The modifications to the basic cavitation approach, modelled by the Rayleigh-Plesset equation, show different behaviour. The introduction of the turbulent pressure oscillation value did not improve significantly the accuracy of the cavitation prediction. On the contrary, the use of the Full Cavitation Model in order to take into account also the gas cavitation due to the presence of non-condensable gas dissolved in the fluid, was found to be an important improvement on the prediction of the cavitation taking place on the upper side of the hydrofoil.

4.2. Arndt Profile

4.2.1. Problem definition

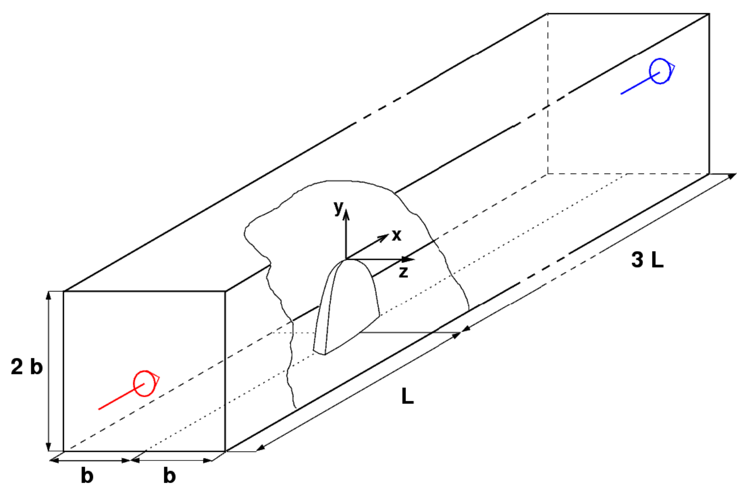

Figure 29: Schematic representation of the NACA 66_2-415 cavitation channel.

In addition to the plano-convex cavitation test, a three dimensional case consisting of a flow around a NACA 66_2-415 hydrofoil with elliptical planform was investigated. In this case tip-vortex cavitation takes place due to the high radial velocity gradients in the vortex tube, which is released from the tip of the hydrofoil. Highly swirling flow generates pressure drop below saturation pressure leading to cavitation on the tip of the hydrofoil and in the vortex core of the tip-vortex.

The test body used in the original facility [1][7] consists of an elliptical planform hydrofoil with a chord length of 81mm, a semispan of 95mm and a mean line of 0.8.
Figure 29 shows the representation of the experimental flow geometry which was exactly used for the CFD simulations as well, while in Figure 30 and Figure 31 the details of the planform geometry of the hydrofoil are pointed out.

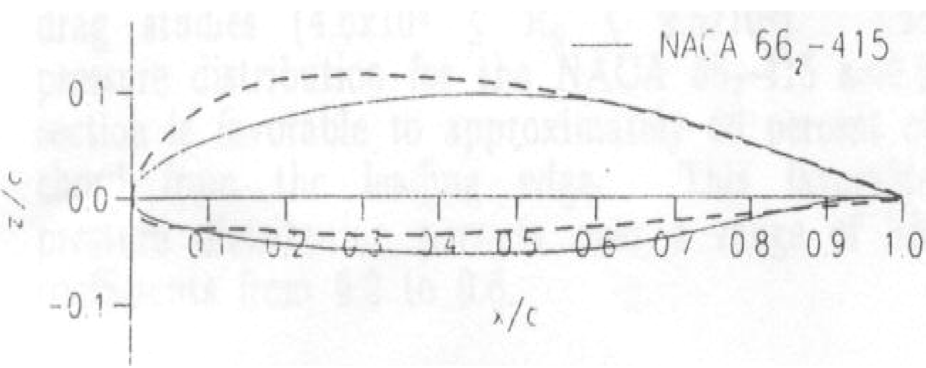

Figure 30: Elliptical profile of the NACA 66$_2$-415.

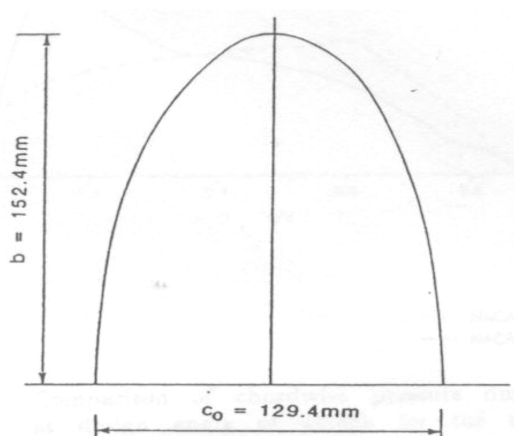

Figure 31: Elliptical profile of the NACA 66$_2$-415.

As for the previous case different configurations were analyzed by changing the angle of attack, the Reynolds number characterising the flow and applying different turbulence modelling approaches (SST, SST with curvature correction term, BSL RSM).
In accordance with the original publication of Arndt an effective angle of attack has been defined as $\alpha_{eff} = \alpha - \alpha_0$, where α_0 corresponds to the zero lift angle, which after a parametric study was chosen as α_0=2.5°.

4.2.2. Boundary/Initial conditions

The boundary conditions to solve this case are analogous as the ones used for the previous case. This means:

- Inlet boundary condition with an inlet velocity value based on the Reynolds number.

$$v_{in} = \frac{\mathrm{Re}\,\mu}{\rho L} \tag{3.7}$$

- Outlet boundary condition with a static outlet pressure based on the cavitation number, vapour pressure and inlet velocity.

$$p_{out} = p_v + \sigma_n \left(\frac{\rho}{2} v_{in}^2 \right) \tag{3.8}$$

- No-slip wall boundary condition for the cavitation tunnel walls and the solids inside the domain. In the same manner as before the CFX automated wall treatment has been applied for turbulence boundary conditions in dependency on y^+ values of the first mesh cell.

4.2.3. Numerical Meshes

The ICEM CFD Hexa grid generator has been used to discretize the domain. A block structure allowing to refine the grid near the blade surface as well as to perform a smooth transition between coarsely resolved areas in the far field and finely resolved areas around the hydrofoil was designed.

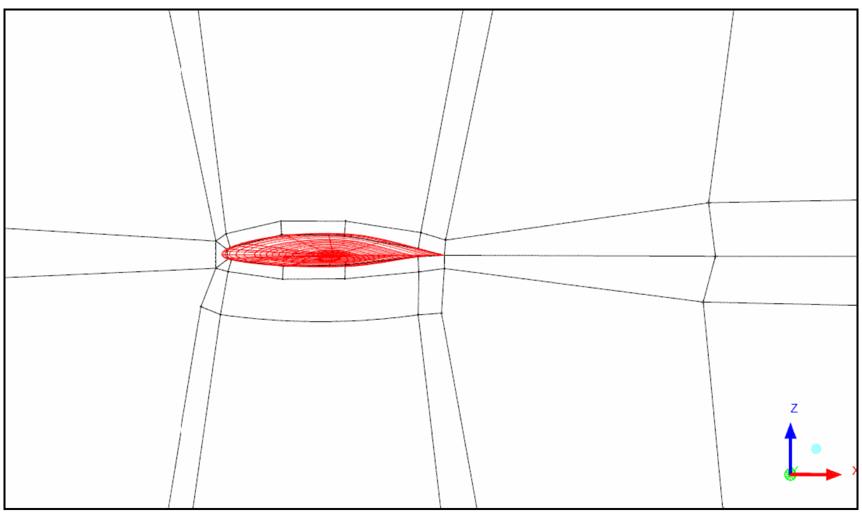

Figure 32: Blocking structure around the hydrofoil.

The resulting blocking structure applied near the hydrofoil is shown in Figure 32, while the coarser mesh obtained with this block structure is presented in Figure 33. The designed grid block structure guarantees a minimum grid angle larger then 20° independent from the grid refinement level. As for the previous case an h-refinement study has been carried out, employing three different grids, which are refined by a factor of $\sqrt[3]{4}$ in each coordinate direction. The same parameters were taken into account to evaluate the quality of the mesh: minimum angle formed by the grid lines, aspect ratios and the near wall distance of the first mesh element (computed as in equation (3.4)). The main information related to the grid properties and grid quality on various mesh levels of refinement used to run the CFD simulations is summarized in Table 3.

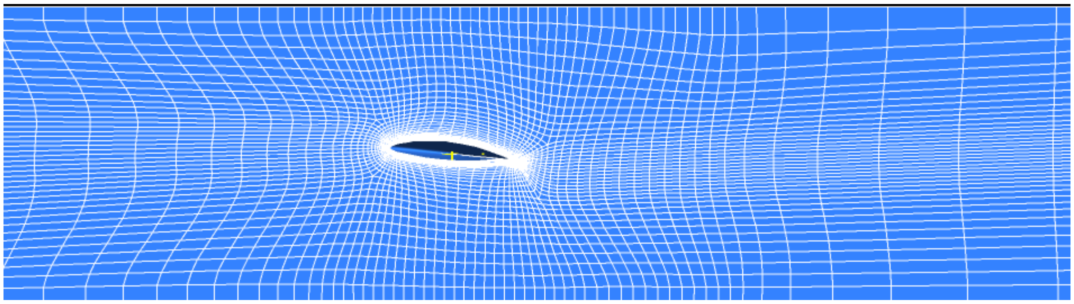

Figure 33: Representation of the meshes employed.

Grid	**Coarse**	**Medium**	**Fine**
# nodes	358.519	1.394.862	5.442.459
# elements	341.596	1.352.603	5.337.217
Minimum grid angle	20.9	20.7	20.1
First layer distance y [μm]	30	15	7.5
Average y^+	14.3	7.1	3.6

Table 3: Grid statistics for the Arndt profile test case.

Test name	**Grid**	**Turbulence Model**
1A	Coarse	**SST**
1B	Coarse	**SST+High Res**
1C	Coarse	**SST+High Res+CC**
1D	Coarse	**BSL-RSM**
2A	Medium	**SST**
2B	Medium	**SST+High Res**
2C	Medium	**SST+High Res+CC**
2D	Medium	**BSL-RSM**
3A	Fine	**SST**
3B	Fine	**SST+High Res**
3C	**Fine**	**SST+High Res+CC**

Table 4: Simulations outline for the Arndt test case.

4.2.4. Computation strategy

Different series of simulations were performed in order to investigate the influence of the grid resolution as well as the influence of the turbulence modeling. Since one of the major difficulties in resolving the flow is the accurate prediction of the swirl motion near the tip of the blade, major attention was paid to it. Not only high resolution schemes were used to solve the turbulent parameter equations, but also a special curvature correction was considered [37]. The summary of the configurations considered is included in Table 4.

4.2.5. Results

4.2.5.1. Resolution of circumferential velocities in the tip

In order to evaluate the quality of the obtained numerical results, the radial velocity profile at different locations has been evaluated. These positions are located near the tip of the hydrofoil and a steep velocity gradient can be observed. Further downstream dissipation of the tip vortex, a reduction in circumferential velocity amplitude as well as in velocity gradient can be observed as the position is departing from the tip. It can be clearly observed in Figure 34, where the velocity profile at the position laying half chord length behind the hydrofoil tip is substantially steeper than the profiles located at a chord length distance or twice chord length distance.

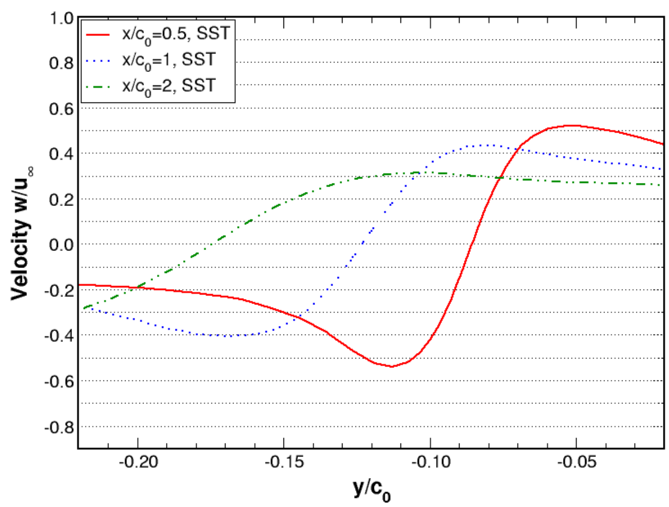

Figure 34: Radial velocity profile at three different locations after the tip vortex for x/c_o=0.5, 1 and 2.

The grid refinement allows to analyze the spatial discretization error of the numerical method and to evaluate if an asymptotical solution independent of the grid resolution can be finally obtained. For this purpose, the radial velocity profile was evaluated using the three refined grids in different locations (Figure 35 and Figure 36). Small differences between the results can be observed even on the highest level of mesh refinement, indicating that a mesh independent solution could not yet be obtained. However, even more severe discrepancies to the experimental results arose, especially on measurement cross section further downstream the hydrofoil where the meshes are coarsening due to axial expansion. While the strong velocity gradients can be predicted for the cross section close to the hydrofoil at x/c_o=0.016, the plotted velocity profiles are much smoother then the experimental data obtained from the experimental facility for x/c_o=1.0 (see Figure 36).

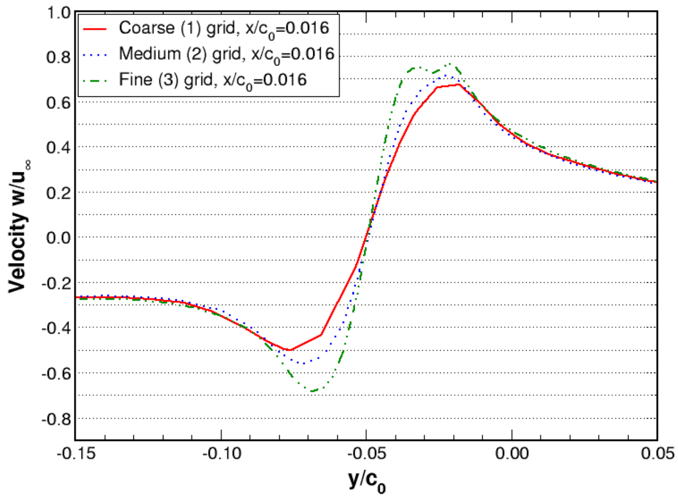

Figure 35: Radial velocity profiles for different grids close to the tip of the hydrofoil.

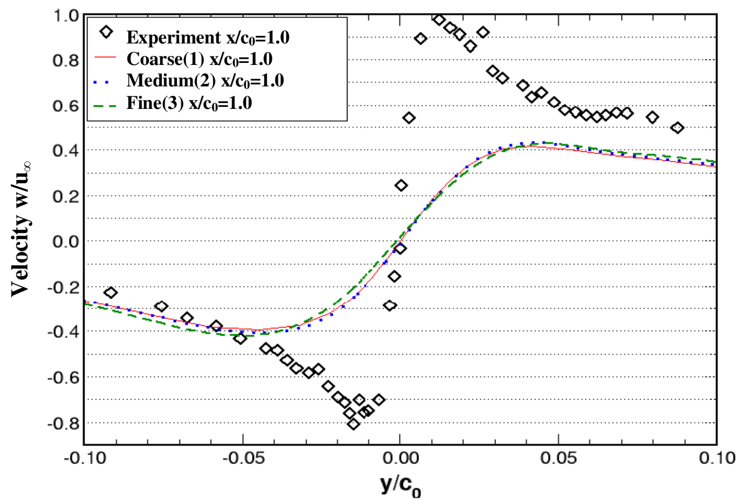

Figure 36: Radial velocity profiles for different grids at a chord length distance from the tip.

A reason for this behaviour is the strong swirl of the velocity field near the tip of the hydrofoil. In order to deal with this effect, different strategies have been considered. The first one consisted of the use of a High Resolution Scheme to solve the turbulence equations, which are solved by default using an upwind advection scheme, which is of cause more diffusive. But the influence of the chosen advection scheme, shown in Figure 37, was found to be not significant. In a second step a curvature correction term in the SST turbulence model had been applied (see section 2.1), in order to account for the strong curvature of streamlines in the tip-vortex flow. The velocity profiles obtained with this curvature correction is also compared in Figure 38, showing an important improvement to approximate the strong velocity gradient.

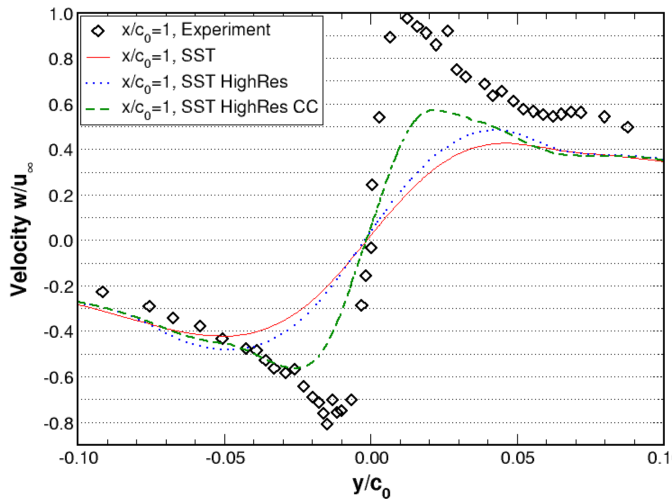

Figure 37: Radial velocity profile with different numerical schemes for solving/modeling the fluid flow turbulence.

A further step was done in order to enhance the evaluation of the velocity gradient near the tip vortex by raising the limitation of assumed isotropic turbulence, which might be not satisfied in the strong swirling flow of the tip vortex behind the hydrofoil. Therefore the turbulence model was changed from a two-equation model (section 0) to the BSL Reynolds Stress Model (section 0), where not two turbulence model equations but one equation for each Reynolds tensor component is solved. In this case, the computer and memory resources required has been increased, but analyzing Figure 38, it can be noticed that even for coarser meshes the enhancement is significant approaching in a more satisfactory comparison of the steep velocity profile to measurement data.

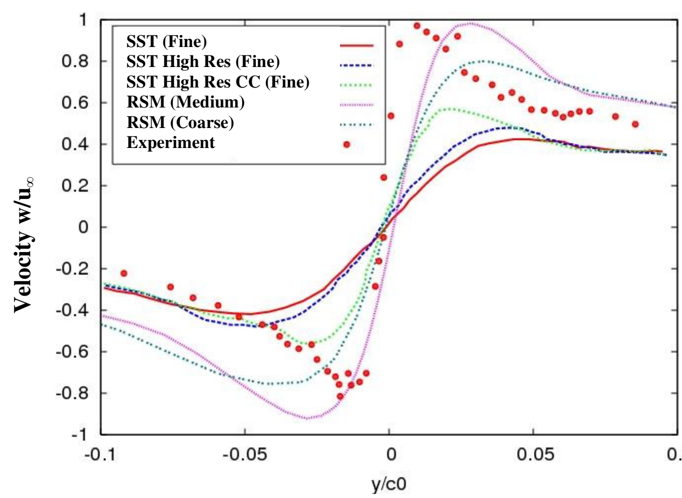

Figure 38: Radial velocity profile for different turbulence modeling at x/c_0=1.

The influence of the turbulence model can also be observed by looking into the vapor volume fraction obtained in an ANSYS CFX multiphase flow simulation applying the cavitation model in combination with SST and BSL RSM turbulence models. A larger tip vortex cavitation zone appears when the BSL Reynolds Stress Model is applied. Sheet cavitation is covering the most of the blade surface for both configurations (Figure 39)

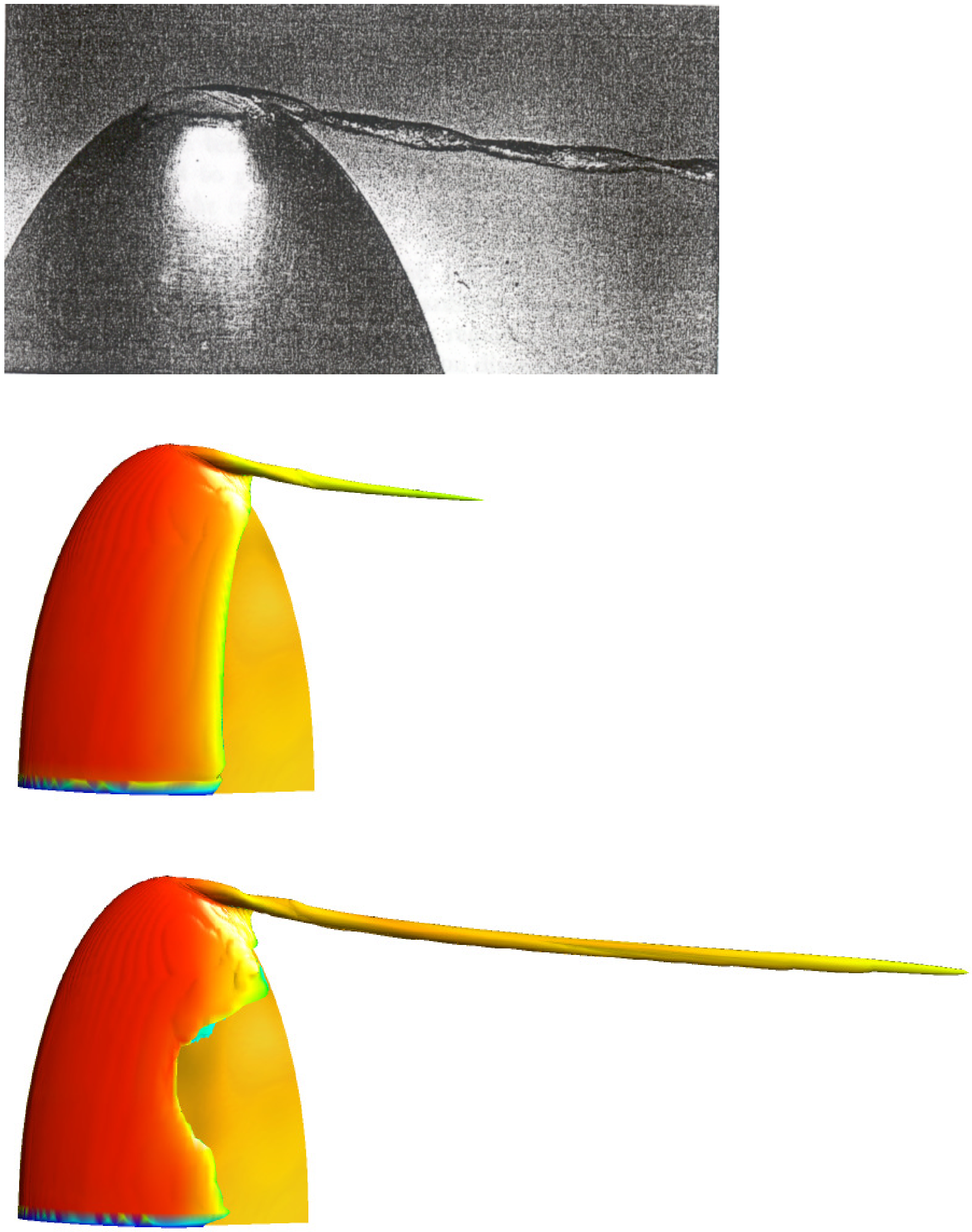

Figure 39: Vapour volume fraction in cavitating flow near the tip. Re=5.2x10^5. σ=0.58. (a) Experimental observation α_{eff}=9.5°, (b) SST turbulence model α_{eff}=12°. (c) BSL Reynolds Stress Model α_{eff}=12°.

4.2.5.2. Tip vortex trajectory

First the shape of the tip vortex trajectory has been investigated. It could be shown that the trajectory does not strongly depend either on the angle of attack, the Reynolds number value or the cavitation number. This effect can be observed in Figure 40, where the tip vortex trajectory obtained for an angle of attack equal to 8.1° and Reynolds number of $9.2x10^5$ is plotted as well as for the case of α=11.6° and Re=$5.2x10^5$ against the experimental values of Arndt.

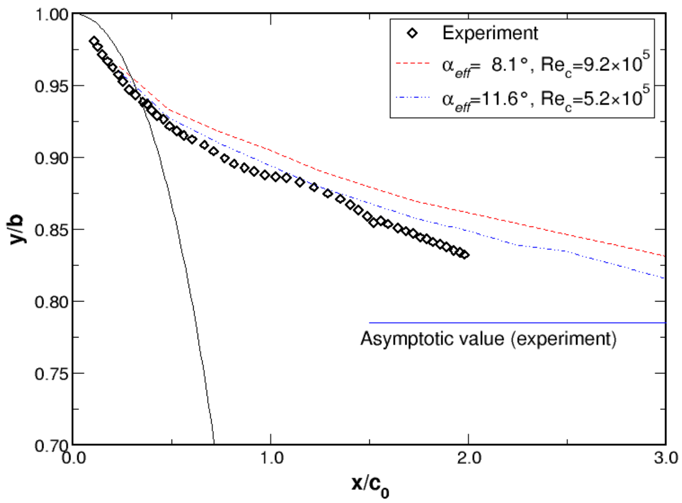

Figure 40: Tip vortex trajectories in the x-y coordinate plane.

4.2.5.3. Lift coefficient

In addition to the tip vortex trajectory and the velocity profiles the value of the lift coefficient, equation(3.6), has been investigated. Figure 41 shows the influence of the angle of attack on the lift coefficient. It has been computed for different Reynolds numbers and by using different grids; however all the computational results are finally arranging between the two experimental results at Obernach [16] and SAFL [7].

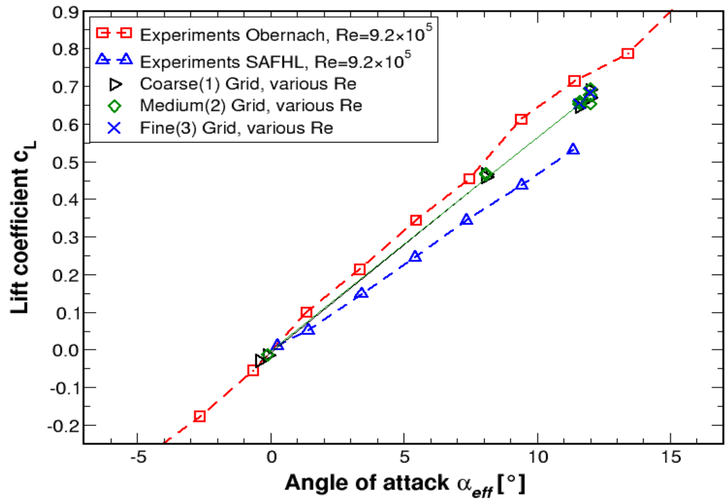

Figure 41: Lift coefficient versus angle of attack.

The relationship between the cavitation inception, the Reynolds number and the lift coefficient has been considered as well. A correlation can be found in literature for the dependency of these three parameters, which is

$$\sigma_i = 0.063\, c_l^2\ \mathrm{Re}^{0.4} \tag{3.9}$$

Results obtained with the three refined grids are compared to the experimental ones, and regressions of the numerical solutions obtained are computed (to compare its slope to the one in equation(3.9)). Figure 42 shows that the slope of the regression curves obtained are lower than the experimental results for the coarse grid, while it increases for the medium grid results. Finally the only result which could be obtained on the finest grid level due to the involved high computational effort is in very good agreement to the experimental results.

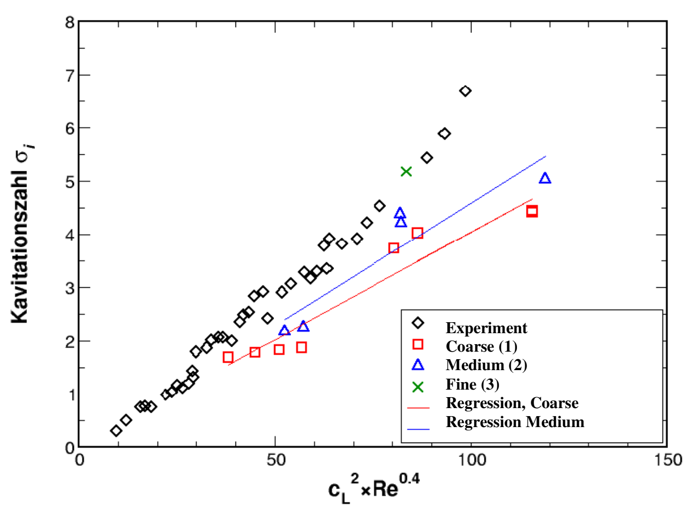

Figure 42: Cavitation inception *vs.* lift coefficient.

4.2.6. Discussion

The test case is based on the experiments by Arndt [1]. Special attention has been paid to the tip vortex, since this is the zone of the flow where larger velocity gradients appear as well as larger pressure drop occurs, originating the inception of the tip-vortex cavitation. The trajectory of the tip vortex and the resolution of the radial velocities in the tip vortex have been investigated and compared to data. The velocity gradients were found to be difficult or expensive to compute and different strategies have been investigated. The basic simulations were run applying the standard SST turbulence model without any modifications, and it has been observed that the use of high order resolution schemes and the use of a curvature correction term in the turbulence model equations improved the resolution of the steep velocity gradient near the tip of the hydrofoil. In addition, a Reynolds Stress Model has been applied showing a more satisfactory agreement to the numerical results even on coarser grids by taking into account the anisotropy of the continuous phase turbulence in the strong swirling flow in the tip vortex behind the tip of the hydrofoil.

4.3. Propeller P1356

4.3.1. Problem definition

The test case analyzed is the flow around a passenger ship propeller called P1356. It has been investigated experimentally as well as numerically. Experiments in model scale were performed in the cavitation tunnel operated at SVA. And the experimental data obtained were afterwards used to validate the numerical simulations performed by using the ANSYS CFX software package.

The propeller in the investigated model scale consists of 5 blades and has a diameter of D=0.25 m. The specific configuration presented here consists of a rotation frequency of n=28 s^{-1}, a propulsion coefficient of J=0.6 and the cavitation number of σ_n=1.816.

The propeller has been investigated inside the cavitation tunnel with a transducer plate located 18 cm above the propeller, where 4 different probes were arranged in a regular pattern on the surface of the plate in order to record transient pressure values at pressure sensor locations. The pressure transducer plate is used in this arrangement as a strongly simplified replacement of a real ship stern model in order to study the propeller/ship hull interaction by propeller rotation, turbulence and cavitation induced pressure fluctuations. Recorded transient pressure signals are then used for the validation of CFD simulation results. Therefore the same propeller configuration and geometry at the same scale was used for the numerical simulations. A schematic representation of the cavitation tunnel located in SVA is shown in Figure 43, and the numerical representation of it including the propeller, the pressure transducer plate arrangement and the probe distribution is shown in Figure 44.

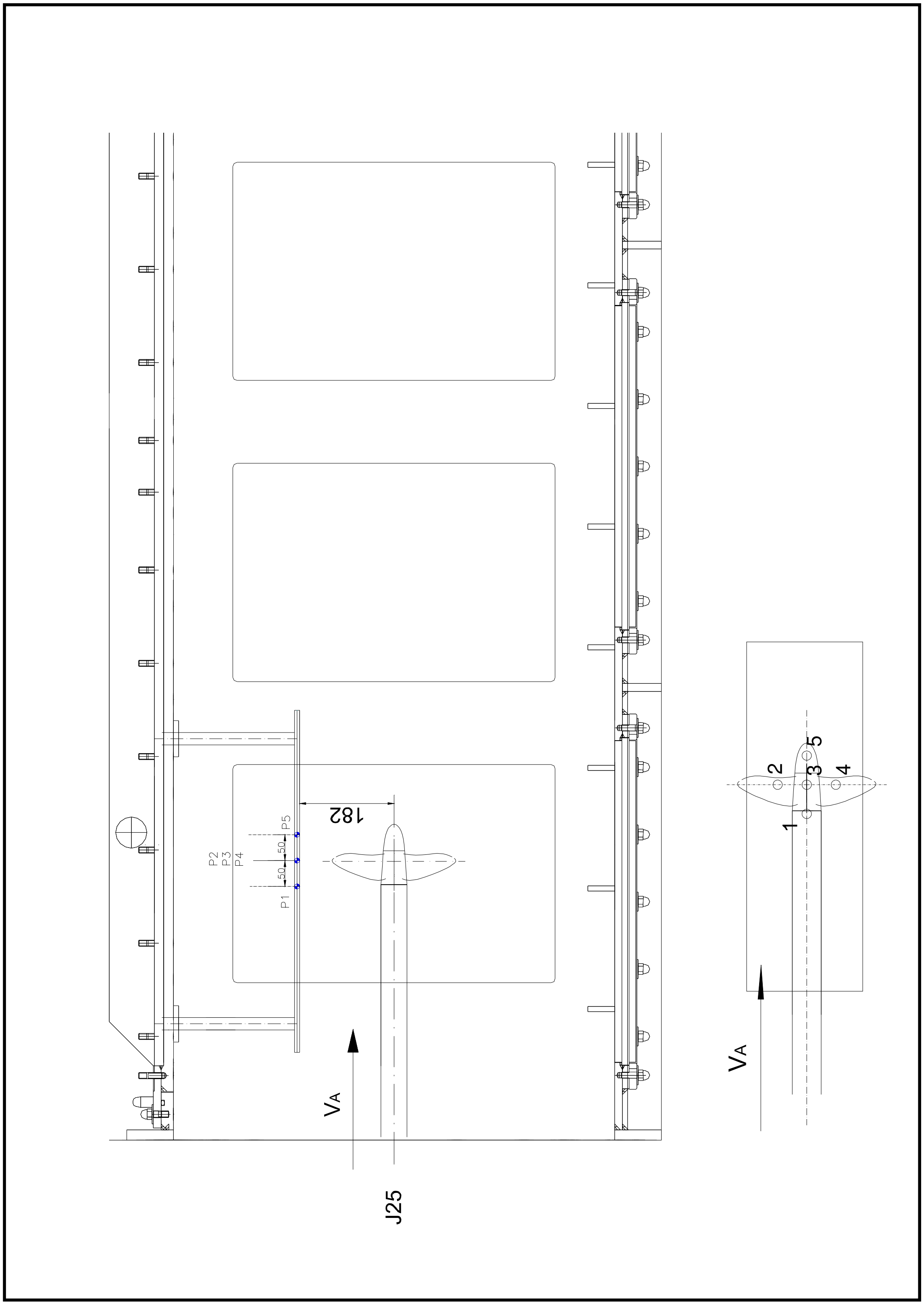

Figure 43: Schematic of the cavitation tunnel at SVA.

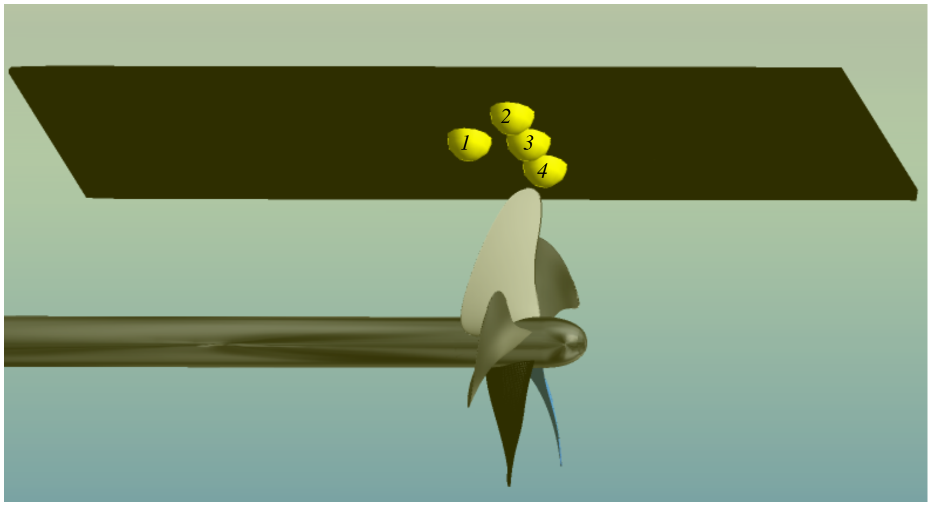

Figure 44: Test case configuration: propeller, transducer plate and probe locations.

The inner cross section of the SVA Potsdam cavitation tunnel is 850x850 mm^2, its maximum flow velocity is 7.5 m/s, the maximum measurable thrust with the used dynamometer is 3000 N and the maximum measurable torque is 150 Nm.
The experimental data were generated after the propeller was rotating for long time, therefore assuring the independency of the recorded data from cavitation tunnel initial state. Then the signal corresponding to 10 cycles was recorded by using Stereo PIV measurements [31]. The camera used has a sensor resolution of 1024x1024 pixels, and it can take from 60 to 2000 Pictures/second using the highest resolution and up to 120000 Pictures/second using the lowest one. The resolution chosen for this case was 6000 Pictures/second containing 512x512 pixels each one.
Regarding the pressure data, transient signals have been recorded with miniaturized pressure sensors of XPM5 type with an adjustable range of measurement between 0-2 bar up to 0-350 bar [32]. For higher reliability of data, clearer plot representation and comparison to CFD results, a statistical average of the data over 10 propeller cycles was obtained.

4.3.2. Boundary/Initial conditions

The simulations computed for this case have been run in a transient mode using a single-phase CFD setup with water under normal conditions as the working fluid. A high resolution numerical scheme has been chosen for the advection term and a second order backward Euler scheme for the transient term.

The following boundary conditions were applied to solve the test case:

- Inlet boundary condition with an inlet velocity value based on the advance coefficient, rotation frequency and propeller diameter.

$$v_{in} = JnD \qquad \textbf{(3.10)}$$

- Outlet boundary condition with a static outlet pressure based on the cavitation number, vapour pressure, rotation frequency and propeller diameter.

$$p_{out} = p_v + \sigma_n \left(\frac{\rho}{2} n^2 D^2 \right) \tag{3.11}$$

- No-slip wall boundary conditions with automatic wall functions for the cavitation tunnel walls and the solids inside the domain.

4.3.3. Numerical Meshes

The domain has been discretized using the mesh generator ANSYS ICEM-CFD [33].It has been split into two parts: one containing the area around the propeller blades (rotating region), and another one for the remaining static part of the domain. This is due to the fact that ANSYS CFX [34] allows running different zones of the domain with either rotor or static frame of reference, and connecting them by using so-called general grid interfaces (GGI) at the rotor/stator interfaces.

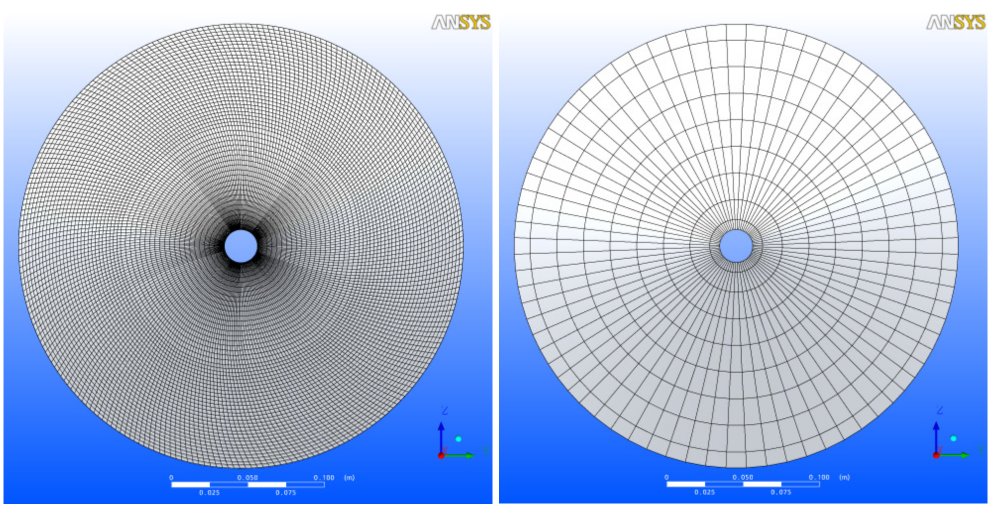

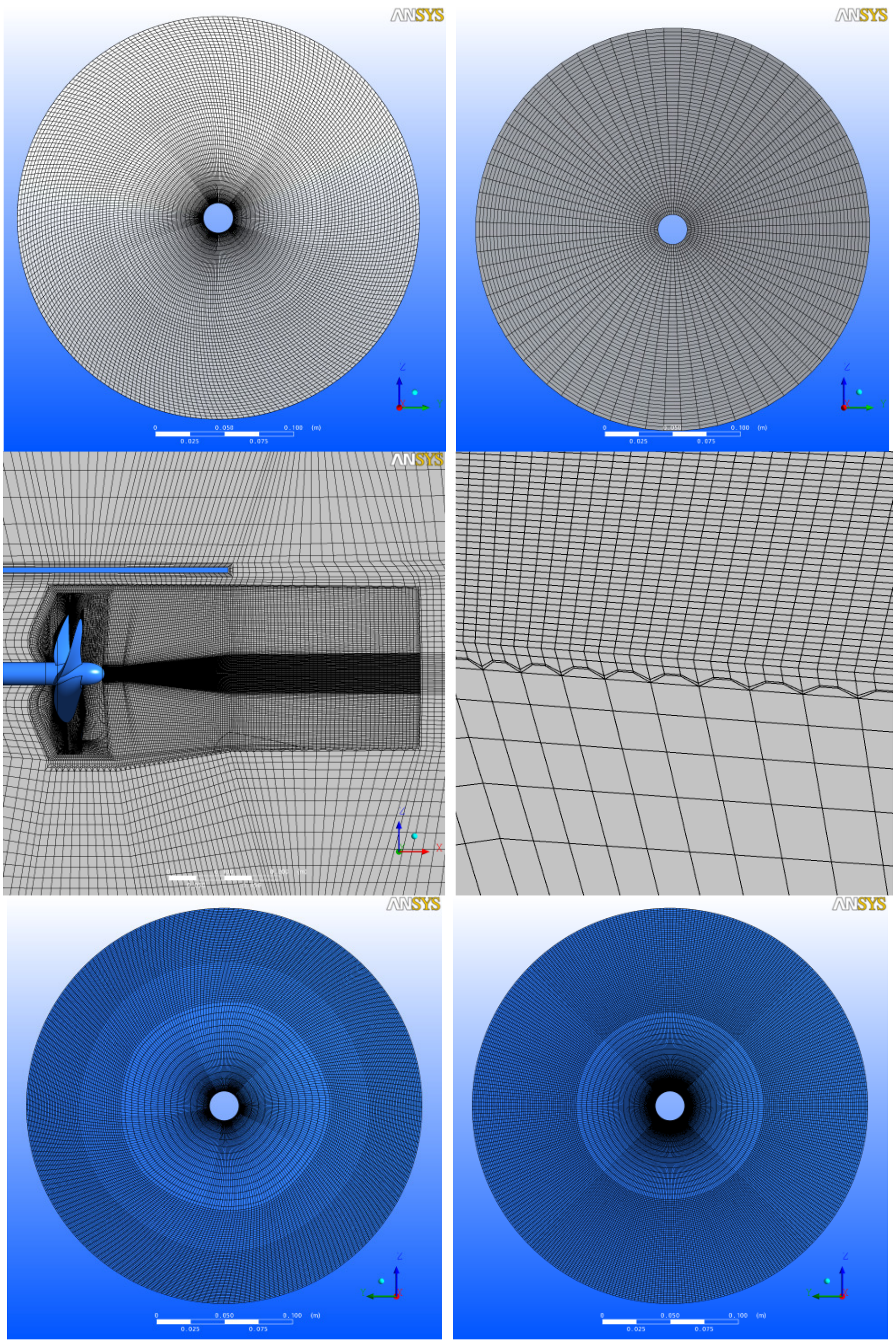

Figure 45: Grid resolution details for different meshes. From top to bottom: Grid 1 (rotor/stator interface); Grid 2 (rotor/stator interface), Grid 3 (structured/unstructured grid coarsening); Grid 5 (rotor/stator interface).

In this way the propeller and a small part of the hub have been simulated in a rotor frame, while the rest of the domain (including the transducer plate) has been simulated in a static frame. As will be explained next, the spatial resolution of the grid at the interface between those two parts plays an important role in order to assure high accuracy of the numerical solutions.

Five different consequently refined grids were investigated (see Figure 45). The first simulation approach (Grid1) contained about 1.4 Mio nodes in total. Due to the skewness of the propeller blades the minimum grid angle was about 9.25 degrees. Due to the generation of a scalable grid structure, this minimum grid angle could be preserved throughout the following steps of grid refinement, thereby assuring a constant mesh quality for all CFD predictions. By analyzing the first simulation results it was pointed out, that the grid resolution at the rotor/stator interface in both domains has a quite significant influence on the CFD simulation results.

Therefore, the second step (Grid 2) consisted of refining the stator in order to get a more similar spatial resolution on both sides of the interface. Even with this approach the grid resolution of the static part of the computational domain was still rather coarse. Refining the grid at the stator domain in order to reach the same resolution as at the rotor side of the rotor/stator interface would imply a propagation of the refinement through the whole stator domain ending up with an enormous amount of nodes and consequently with a much too high computational effort for the computational flow prediction.

Therefore the third grid (Grid3) avoids this grid refinement propagation by applying a new feature of the ANSYS ICEM-CFD Vers. 11.0 grid generator [35]. It allows generating a non-structured layer that creates a smooth transition between a densely refined zone of the grid and a coarser one (Figure 45). This way only a minor part of the stator (the one just after the interface, where the system of tip vortices is propagating downstream of the propeller) is refined, resulting in a similar spatial resolution on both sides of the rotor/stator interface. The fourth mesh uses the same meshing strategy but nodes in the refined part of the stator domain are more concentrated in the area where the tip vortices departing from the blades are supposed to propagate. The final grid (Grid5) is a refinement of the previous one including an extension of the zone right after the interface where the grid is refined. The main characteristics of the grids used for the numerical simulations are summarized in Table 5.

	Nodes at rotor domain	**Nodes at stator domain**	**Min grid angle**
Grid1	1.159.050	270.460	9.25º
Grid2	1.159.050	605.620	9.25º
Grid3	1.159.050	3.117.222	9.25º
Grid4	1.196.825	3.847.814	9.00º
Grid5	1.627.550	8.464.877	9.90º

Table 5: Grid statistics for the propeller case.

4.3.4. Computation strategy

In order to investigate the influence of the two parameters (grid resolution, and turbulence modeling) different configurations were analyzed. Their description is summarized in Table 6. Besides the application of turbulence viscosity based URANS models, for the sufficiently refined numerical grids 3-5 also scale-resolving turbulence modeling (SAS-SST and DES) has been applied in the numerical simulations in order to reproduce the flow structure of detaching tip vortices correctly.

Test name	Grid	Turbulence Model
1A	1	**SST**
1B	1	**SST+CC**
1C	1	**BSL-RSM**
2A	2	**SST**
2B	2	**SST+CC**
2C	2	**BSL-RSM**
2D	2	**EARSM**
3A	3	**SST**
3B	3	**SST+CC**
3C	3	**BSL-RSM**
3D	3	**EARSM**
3E	3	**SAS-SST**
4E	4	**SAS-SST**
4F	4	**DES**
5F	**5**	**DES**

Table 6: Simulations outline for the propeller case.

4.3.5. Results

Two main characteristics or target properties have been analyzed in order to evaluate the results obtained with respect to the different grids and different turbulence models, which are the transient, ensemble averaged pressure signals at the probes located on the transducer plate and the tip vortex structure of the flow departing off the tips of the propeller blades and propagating downstream the cavitation tunnel behind the propeller. The first ones can be compared to recorded pressure data from the CFD simulations (Figure 46, Figure 47, Figure 48), while the second ones can be compared to visual observations and movies obtained directly from high-speed camera at the cavitation tunnel at SVA (Figure 49,Figure 50).

4.3.5.1. Transient pressure signals

The influence of the turbulence modeling can be observed in Figure 46. On its top, the transient pressure signal at the probe number 2 for the *1A/1B/1C* configurations is shown. Results show that for the Baseline Reynolds Stress Model (BSL RSM) approach the phase and the amplitude of the pressure signal is in better agreement with the experimental data then for the case using the standard SST w/o curvature correction (CC), as could be expected, since it represents the more accurate turbulence model and accounts for anisotropy of swirling flows.

The middle diagrame contains the transient pressure signal for the *2B/2C/2D* configurations. In this case, the phase and amplitude prediction of the pressure signal is similar for the different models. There is no shift on the phase of the profiles, and the EARSM and the BSL-RSM show a very similar performance.

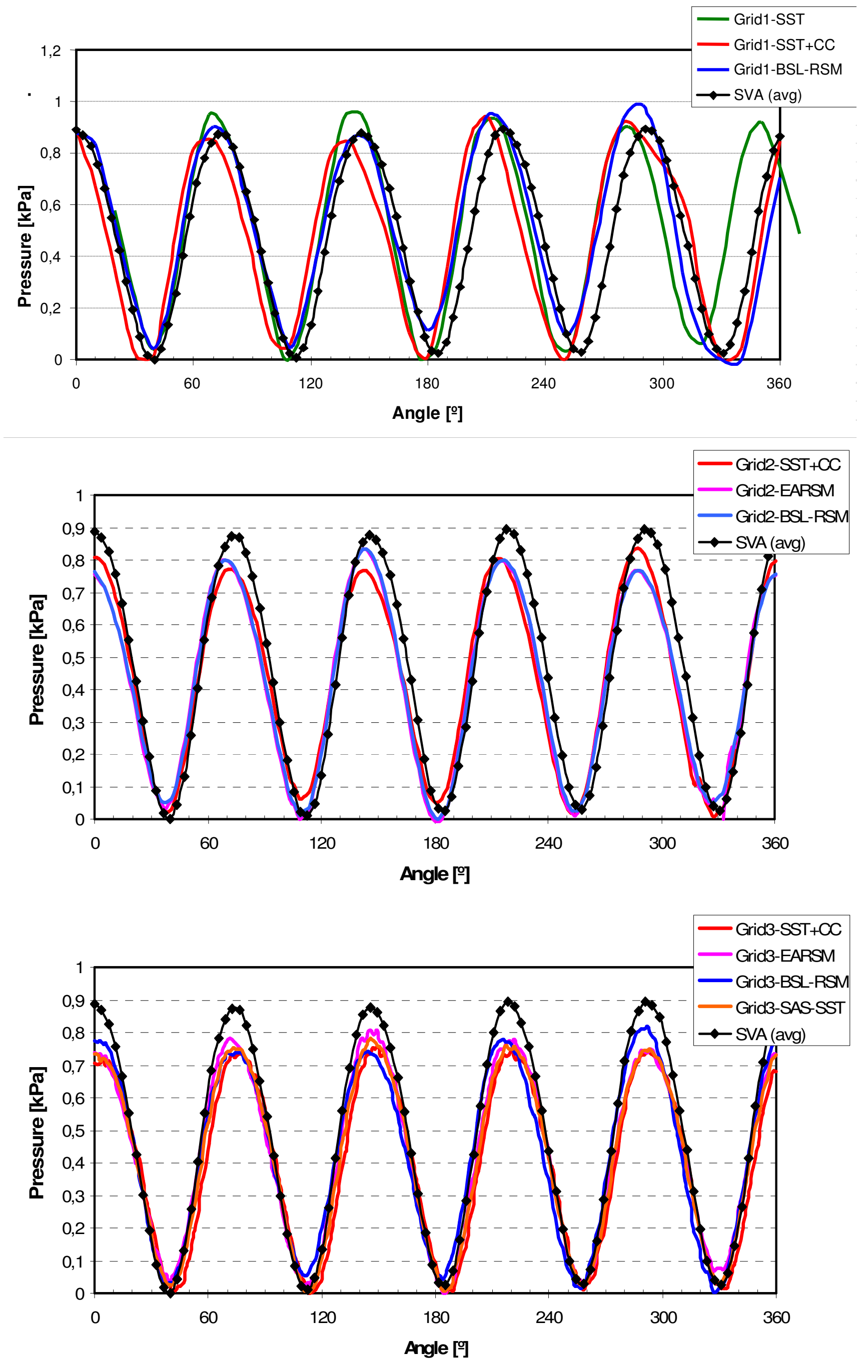

Figure 46: Transient pressure signal at probe 2 for different turbulence models. Top: Grid 1; Middle: Grid 2; Bottom: Grid 3.

Results on the bottom correspond to the 3B/3C/3D/3E simulations. The same qualitative behavior can be observed. The influence of the grid resolution can be noticed in Figure 47. Results for the second probe, in this case for the simulations 3E/4F/5F, are compared again to the experimental data. No significant difference between the fourth grid results and the third grid results is observed, as expected since the number of grid nodes is of the same order, grid resolution of the rotor domain is the same and only the location and number of nodes inside the stator domain is changed. However, when the results on the 8.5 Mio nodes grid are analyzed (grid 5), it can be seen that the CFD simulations predict highly satisfactory the experimental results, even reaching the same amplitude level. The last grid 5 contains more than twice the amount of nodes than the previous one (grid 4).

For the sake of briefness not all results corresponding to the other three probes are included. The qualitative results are the same, and the same trends were observed. Just the results for the case 5F (Grid 5, solved with the DES turbulence model), are shown (Figure 48).

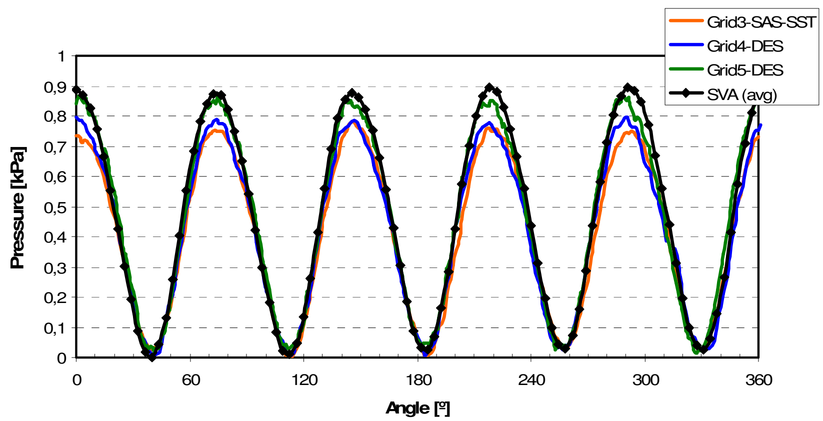

Figure 47: Transient pressure signal at probe 2 . Case 3E, 4F, 5F.

The transient pressure signals at the second and fourth probe are in good agreement with the experimental data, and only for the third one the discrepancies are larger.

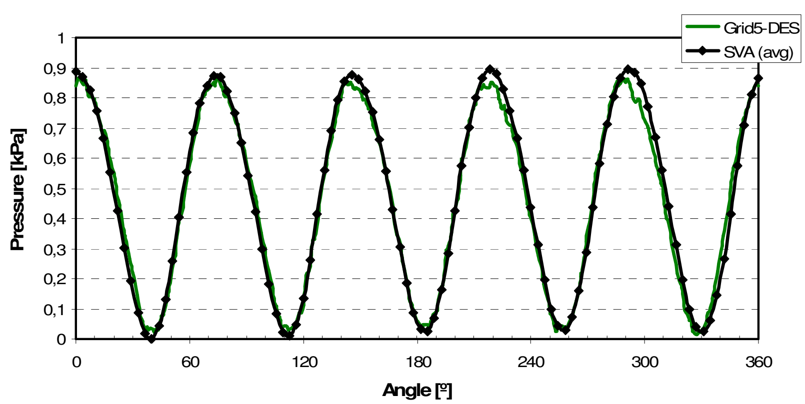

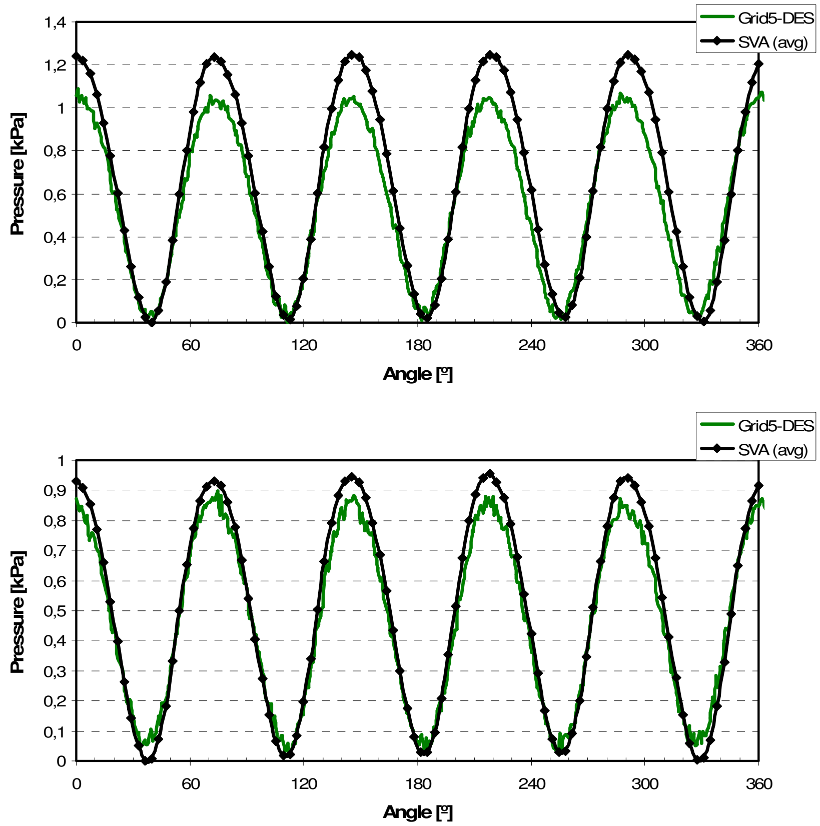

Figure 48: Transient pressure signal. Case 5F. Top: probe 2; Center: probe 3; Bottom: probe 4.

The accurate prediction of the pressure field leads in turn to an accurate prediction of local pressure oscillations and the formation of cavitating zones due to locally decreasing pressure below the saturation pressure of the fluid. It was found that it was necessary to use the finest grid and more accurate scale-resolving turbulence model to reproduce the experimental values. However, by comparing only the transient pressure signal, it could be thought that the difference between, for instance, grid 3 and 4 is not of large importance. Pictures presented in next section show, that besides the achieved accuracy of the transient pressure signals special effort has to be undertaken in order to reproduce the details of the flow structure behind the propeller.

4.3.5.2. Influence of the GGI Improvements and Tip vortex prediction

Since the final goal of the presented CFD study is the prediction of cavitation and the locations at the propeller blade surfaces where cavitation inception will take place, the structure of the flow was investigated. Flow and vortex structure was analyzed more thoroughly by visualization of isosurfaces of the pressure field and turbulence related quantities.

In Figure 49 pressure isosurfaces for the five analyzed grids are plotted. Results correspond to the most accurate turbulence model in each case, so BSL RSM for grids 1-3 and DES for grids 4-5. The visualized domain includes the rotor including the propeller blades and the area in downstream direction. Black lines on the pictures represent the discretization of the rotor/stator interface from the rotor point of view.

It was clearly found, that the first grid contained a too significant different resolution on both sides of the rotor/stator interface. Therefore a significant amount of information was lost at the rotor/stator interface due to interpolation errors. This can be noted because the tip vortices departing from the blades suddenly disappear on the interface location. The diffusion due to the interpolation between rotating and static parts of the computational domain does not allow them to cross the interface.

The second grid was refined in the circumferential direction in order to get a more similar spatial resolution on the mentioned interface. A slight improvement could be observed, because now the tip vortices cross the interface, but only a very short distance, almost insignificant. This indicated that the refinement was not still not sufficiently high, especially on the stator part of the domain adjacent downstream of the rotor domain. Thus, the necessity of a new meshing strategy arose.

The third grid simulation shows a notable progress in this sense. The isosurface length is larger, crossing the interface without loosing information. However, it looked not long enough as in the experimental facilities. In this case an optimization of the local node density was required, which was achieved by reallocation of nodes to the region, where the tip vortices propagate from the rotor domain into the stator domain keeping the overall number of nodes on the mesh almost constant.

The numerical results obtained with the fourth grid are more adequate in terms of tip vortices length prediction. The issue at the interface is totally fixed, and the characteristics of the results depend now on the global mesh parameters. However, some non-physical gaps in the lateral vortex structures appeared. This effect was not due to any deficiencies of the physical modeling but is related to the fact of non-appropriate projections of the edges of grid blocks in the far field behind the propeller. Larger cell sizes in the corners of rectangular grid block structures lead to a local coarsening of the numerical mesh with increasing distance to the rotor of the propeller and therefore to a deterioration in spatial resolution, which caused the tip vortices to disappear locally.

By fixing this meshing issue in grid 5 and by enlarging the area just behind the rotor/stator interface where the grid is refined, a very satisfactory result in agreement with the experimental observations was achieved. The pressure isosurfaces visualizing the location of the tip vortices show now a very comparable shape in comparison to the cavitation tunnel observations.

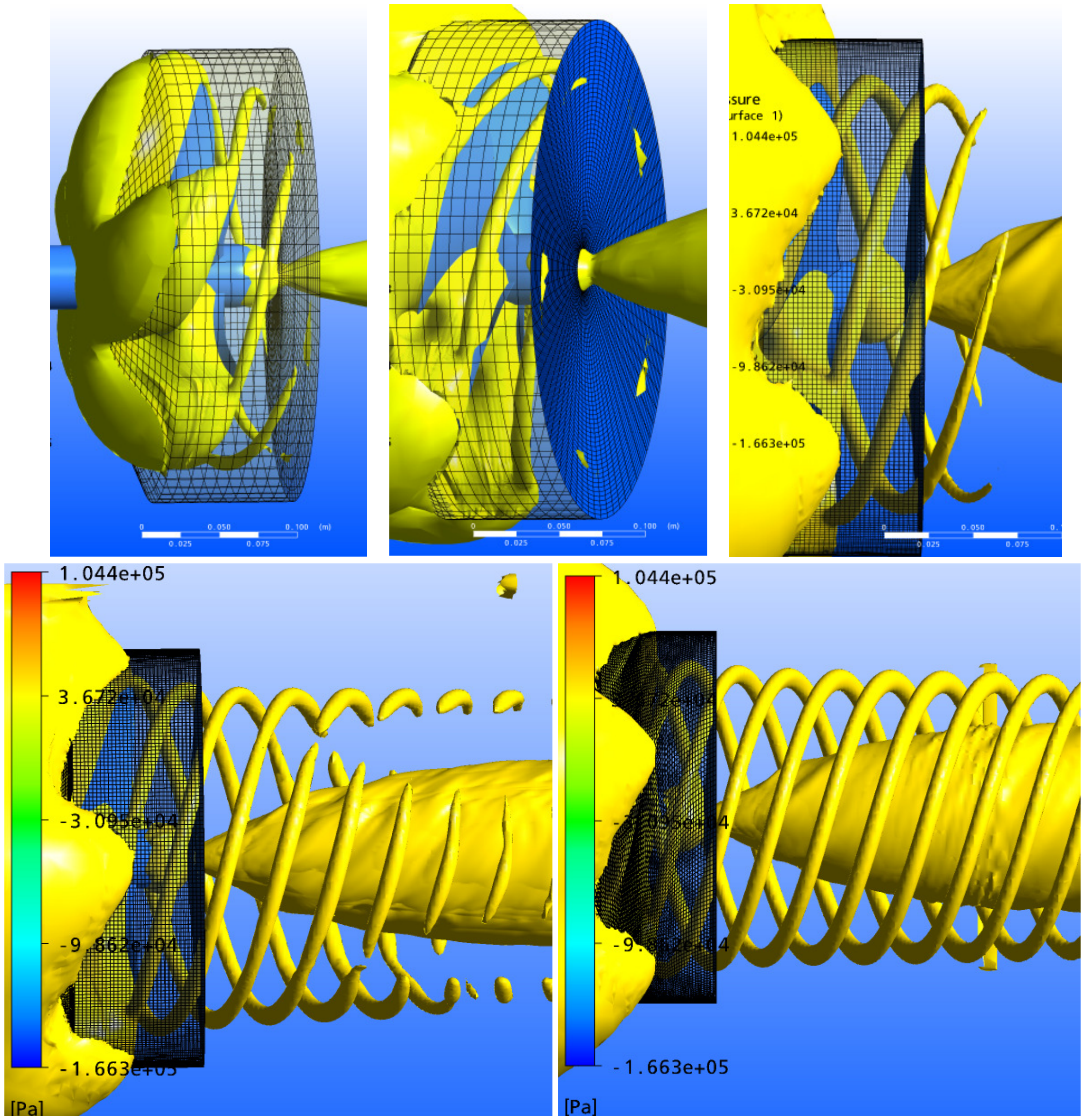

Figure 49: Pressure isosurface (P=47KPa) for the different grids. Top left: Case 1C; Top middle: Case 2D; Top right: 3F; Bottom left: Case 4F; Bottom right: Case 5F.

Since the resolution of the cavitation has an intrinsic relation with the degree of turbulence resolution, turbulence quantities can help us for the study and visualization of the flow structure. In this way, the so called Q-criteria value was analyzed. It is a velocity gradient invariant considering the vorticity and shear strain rate of the flow. It can be mathematically described as

$$Q = \Omega^2 - S^2 = \left(\frac{\partial u_i}{\partial x_j} - \frac{\partial u_j}{\partial x_i} \right)^2 - \left(\frac{\partial u_i}{\partial x_j} + \frac{\partial u_j}{\partial x_i} \right)^2 \qquad \textbf{(3.12)}$$

This value has units of [s^{-2}]. In order to deal with a dimensionless parameter a modification of it was used. It has been done considering one of the more significant values characterizing the configuration of the flow, which is the rotation frequency of the propeller (*n*).

$$Q^* = Q/n^2 \qquad \textbf{(3.13)}$$

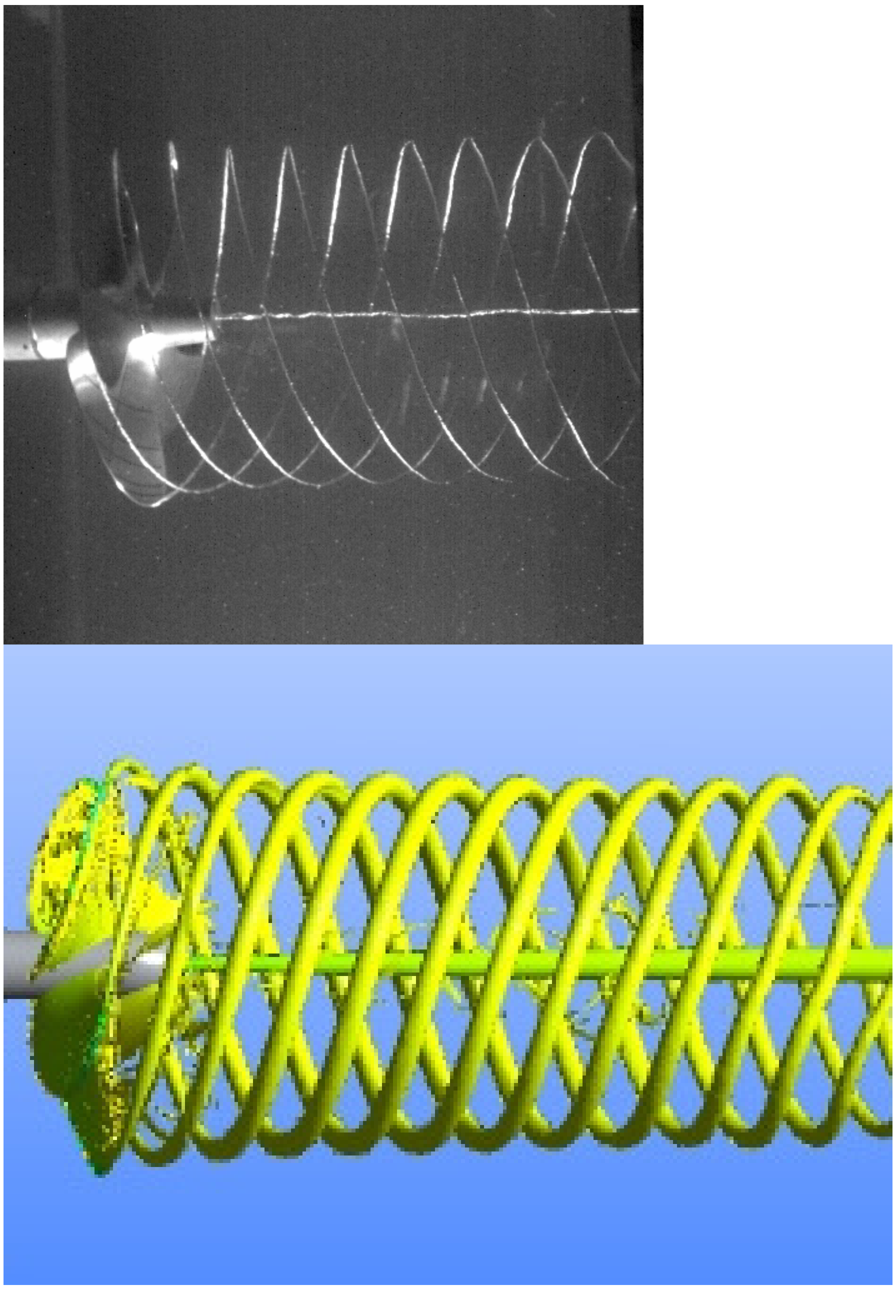

Figure 50: Top: Propeller at the cavitation tunnel at SVA;
Bottom: Q^*-criteria isosurface obtained with numerical simulation, case 5F (Q^*=60).

In Figure 50 there is a qualitative comparison between a snapshot of the cavitation tunnel while the propeller is rotating (top) with the same parameters defined in the numerical simulations, and a plot of a Q^*-criteria isosurface obtained with the finest grid and DES model. It can be noted that the degree of agreement is fully satisfactory in terms of predicted flow structure behind the propeller.

4.3.6. Discussion

The study of a flow around a ship propeller by means of CFD simulations was carried out. This kind of flows are of large interest for the marine industry, and usually very costly when analyzed experimentally.

The main focus of the investigations was two-fold: to study the influence of grid resolution and turbulence modeling on transient pressure oscillations caused by the propeller flow and on the flow structure downstream of the propeller.

Therefore, different grids and turbulence models were considered. Both of them were found to have an important influence on the accuracy of the numerical solution, especially with respect to the spatial and timely resolution and downstream propagation of tip vortex structures departing from blade tips of the propeller.

Numerical results were compared to experimental data obtained from scaled model experiments at SVA Potsdam test facilities. With the finest grid and by applying a scale-resolving DES turbulence model very satisfactory agreement between numerical predictions and experiments could be observed, in terms of transient pressure signal predictions at given measurement locations and in terms of the predicted and visually observed flow structure behind the propeller blades.

The information obtained from the presented and discussed single-phase simulations indicate, that a multiphase simulation applying a cavitation model would require even finer grids in order to resolve the small geometrical structures of tip vortices and consequently the drop of the local pressure in tip vortices below the saturation pressure, which finally would lead to the tip vortex cavitation observable in the experiments. Nevertheless the developed methodology of investigation using scale-resolving SAS-SST or DES simulation can be used to acquire very useful information about cavitation endangered parts of a propeller design even upfront a cavitation simulation by carrying out single phase simulation only and by investigating the turbulence induced patterns of pressure minima in the flow field.

5. Conclusions

A model in ANSYS CFX to deal with cavitation phenomena has been developed. It is based on a homogeneous multiphase flow approach and on modelling of the bubble dynamics solving the Rayleigh-Plesset equation for cavitation bubble radius. The model has been combined with different turbulence models for the continuous fluid phase. Turbulent pressure fluctuations and their influence on the cavitation phenomena were taken into account by relating them to the turbulent kinetic energy of the continuous phase. As a further step, also the presence of non-condensable gases has been modelled, by means of the so-called Full Cavitation Model.

The study of a flow around a two-dimensional plano-convex hydrofoil (Le profile), a three-dimensional elliptical hydrofoil (Arndt profile) and a ship propeller P1356 by means of CFD simulations was presented. The increase of the difficulty in the test cases investigated allowed us to perform a deep analysis of the phenomena. This kind of flows are of large interest for the marine industry, and usually very costly when analyzed experimentally.

The main focus of the investigations in all cases was two-fold: to study the influence of grid resolution and turbulence modeling on transient pressure oscillations caused by the propeller/hydrofoil flow and on the flow structure downstream of it. The developed CFD models have been validated against experimental data for all 3 testcases.

Therefore, different grids and turbulence models were considered. Both of them were found to have an important influence on the accuracy of the numerical solution, especially with respect to the spatial and timely resolution and downstream propagation of tip vortex structures departing from blade tips of a static hydrofoil or the propeller.

For the first case, three refined grids have been used for the simulation, ensuring comparable mesh quality on all grid levels. The cavitation lengths, pressure coefficients and lift values have been investigated and compared against the literature values. The numerical results agree reasonably well to the experiments, even the necessity to use even finer grids could be shown from the present validation study.

The second test case is based on the experiments by Arndt. Special attention has been paid to the tip vortex, since this is the zone of the flow where larger velocity gradients appear as well as larger pressure drop occurs, originating the inception of the tip-vortex cavitation. The trajectory of the tip vortex and the resolution of the radial velocities in the tip vortex have been investigated and compared to data. The velocity gradients were found to be difficult as well as expensive to compute and different strategies have been investigated. The basic simulations were run applying the standard SST turbulence model without any modifications, and it has been observed that the use of high order resolution schemes and the use of a curvature correction term improved the resolution of the steep velocity gradient near the tip of the hydrofoil. In addition, a Reynolds Stress Model has been applied showing a more satisfactory agreement to the numerical results even on coarser grids by taking into account the anisotropy of the continuous phase turbulence in the strong swirling flow in the tip vortex behind the tip of the hydrofoil.

For the propeller case, numerical results were compared to experimental data obtained from scaled model experiments at SVA Potsdam test facilities. With the finest grid and by applying a scale-resolving DES turbulence model very satisfactory agreement between numerical predictions and experiments could be observed, in terms of transient pressure signal predictions at given measurement locations and in terms of the predicted and visually observed flow structure behind the propeller blades.

The information obtained from the presented and discussed single-phase simulations indicate, that a multiphase simulation applying a cavitation model would require even finer grids in order to resolve the small geometrical structures of tip vortices and consequently the drop of the local pressure in tip vortices below the saturation pressure, which finally would lead to the turbulence induced tip vortex cavitation observable in the experiments.

With respect to the pressure fluctuations measured on the simplified ship stern surface (in the simplified cavitation tunnel experiments represented by the pressure transducer plate) a very satisfactory agreement between the CFD simulation data and the experimental data from the pressure transducer measurements could be obtained with the derived CFD simulation technology. This offers encouraging possibilities for the application of CFD for the investigation of pressure fluctuations on ship sterns in full scale and in dependence on real propeller and rudder designs.

6. Publications

- Jebauer S., “Numerische Simulation kavitierender Strömungen”, Diploma Thesis, TU Dresden, pp. 1-79 (2006).

- M. Kuntz, Th. Frank. "CFD Simulation of Cavitating Flows over Hydrofoils" *24th CADFEM & ANSYS CFX Users Conference* 25.-27. Oktober 2006, Schwabenlandhalle Stuttgart/Fellbach, Germany.

- Lifante, C., Frank, T., Kuntz, M, 2007, „Extension and Validation of the CFX Cavitation Model for Sheet and Tip Vortex Cavitation on Hydrofoils”, *5th Joint FZR & ANSYS Workshop "Multiphase Flows: Simulation, Experiment and Application"*, Dresden.

- Frank, T., Lifante, C., Rieck, K, 2007, „CFD Simulation of Cloud and Tip Vortex Cavitation on Hydrofoils”, *Proceedings of the International Conference on Multiphase Flow*. ICMF 07, Leipzig.

- Lifante, C., Frank, T., Rieck, K, 2007, “Investigations of Pressure Fluctuations caused by Turbulent and Cavitating Flow around a P1356 Ship Propeller“, *Proceedings of the ANSYS Conference & 25 CADFEM Users Meeting*. ACUM07. Dresden.

- Lifante, C., Frank, T., Rieck, K, 2008, “Investigation of Pressure Fluctuations caused by Turbulent and Cavitating Flow around a P1356 Ship Propeller”. Proceedings of the NAFEMS Seminar: Simulation komplexer Strömungsvorgänge (CFD)”. Wiesbaden, Germany.

- Lifante, C., Frank, T., Rieck, K, 2008, “Investigation of Pressure Fluctuations caused by Turbulent and Cavitating Flow around a P1356 Ship Propeller”. Proceedings of the Marine CFD 2008. Southampton, UK.

- Lifante, C., Frank, T., Rieck, K, 2007, “Investigations of Pressure Fluctuations caused by Turbulent and Cavitating Flow around a P1356 Ship Propeller“, *Proceedings of the ANSYS Conference & 3 CADFEM Austria Users Meeting*. 2008. Wien. Austria.

- Lifante, C., Frank, T., Rieck, K, 2008, “On influence of turbulence modeling on cavitation prediction for flow around P1356 ship propeller”. Proceedings of the 27th International Conference on OFFSHORE MECHANICS AND ARCTIC ENGINEERING (OMAE 2008), June 15-20, 2008. Estoril, Portugal.

7. Nomenclature

D	Propeller diameter
n	Rotation frequency
J	Propulsion coefficient
σ_n	Cavitation number
r	Phase volume fraction
u_i	Velocity component (m s^{-1})
$\dot{S}$	Mass transfer rate (Kg m^{-3} s^{-1})
g_i	Gravity component (m s^{-2})
P	Pressure (N m^{-2})
c_p	Pressure coefficient
c_L	Lift coefficient
A	Area
F	Force
L	Characteristic length
Re	Reynolds number
P_k	Turbulence kinetic energy production
F_{vap}	Vaporisation factor
F_{cond}	Condensation factor
$\overline{u}_i$	Average velocity component (m s^{-1})
$u_i^{'}$	Fluctuating velocity component (m s^{-1})
k	Kinetic energy (m^2 s^{-2})
Ω	Vorticity
S	Shear Strain Rate
v_{in}	Inlet normal velocity
p_{out}	Outlet static pressure
Q	Q-criteria value
$Q*$	Dimensionless Q-criteria value

Greek letters

ε	Turbulence dissipation rate (m^2 s^{-3})
ω	Turbulence frequency (s^{-1})
ρ_α	Phase density (Kg m^{-3})
τ_{ij}	Stress tensor component (Kg m s^{-2})
σ	Surface tension coefficient (m^3 s^{-2})
α	Angle of attack
α_0	Zero lift angle

Subscripts

m	Mixture
v	Vapour
l	Liquid

α	Phase
sat	Saturation
in	Inlet
out	Outlet
eff	Effective
L	Lift
nuc	Nuclei

8. References

[1] Arndt, R.E.A., Dugue, C., “Recent Advances in Tip Vortex Cavitation Research”, Proc.The International Symposium on Propulsors and Cavitation, Hamburg, Deutschland, 22.-25. Juni, 1992.

[2] Franc J.P., “Partial Cavity Instabilities and Re-Entrant Jet”, Keynote Lecture 002, Proc. 4th International Symposium on Cavitation, Pasadena, Kalifornien, U.S.A., 20.-23. June 2001.

[3] Jebauer S., “Numerische Simulation kavitierender Strömungen”, Diploma Thesis, TU Dresden, pp. 1-79 (2006).

[4] Le Q., Franc J.P. und Michel J.M., Partial Cavities: “Global Behavior and Mean Pressure Distribution”, Journal of Fluids Engineering, Vol. 115-2, S. 243-249 .1993.

[5] Menter F., “Two-Equation Eddy-Viscosity Turbulence Models for Engineering Applications”, AIAA Journal, Vol. 32, No. 8, pp. 1598-1605 (1994).

[6] Menter F., “CFD Best Practice Guidelines for CFD Code Validation for Reactor Safety Applications”, ECORA Project, pp. 1-47 (2002).

[7] Arndt, R.E.A. and Arakeri, V.H., Higuchi, H., 1991, “Some observations of tip-vortex cavitation“, J. Fluid Mechanics, Vol. 229, pp. 269-289

[8] Maines, B.H. and Arndt, R.E.A., 1997, “Tip Vortex Formation and Cavitation“, J. Fluids Eng., Vol. 119-2, pp. 413-419

[9] Abbot, I.H. and Doenhoff, A.E. von, 1959, “Theory of Wing Sections”, Dover

[10] Maines, B.H., 1995, “Tip Vortex Formation and Cavitation“, Dissertation, University of Minnesota, U.S.A.

[11] B., Takacs, T., Willemsen, S., 2001, “CFD Best Practice Guidelines for CFD Code Validation for Reactor-Safety Applications”, European Commision, ECORA

[12] Casey, M., Wintergerste, T., 2000, “Best Practice Guidelines, ERCOFTAC Special Interest Group on Quality and Trust in Industrial CFD”, Fluid Dynamics Laboratory Sulzer Innotec, 94 p.

[13] Wilcox, D.C., “Multiscale model for turbulent flows”, In AIAA 24th Aerospace Sciences Meeting. American Institute of Aeronautics and Astronautics, 1986.

[14] Menter, F.R., “Multiscale model for turbulent flows”, In 24th Fluid Dynamics Conference. American Institute of Aeronautics and Astronautics, 1993.

[15] Menter, F.R., and Egorov, Y. “A Scale-Adaptive Simulation Model using Two-Equation Models”, AIAA paper 2005-1095, Reno/NV, 2005.

[16] Kjedsen, M. Arndt, R.E.A., Effertzt, M. “Spectral Characteristics of Sheet/Cloud Cavitation”. Journal of Fluids Engineering. Vol 122. 2000. pp 481-487

[17] Menter, F., Hemstrom, B., Henriksson, M., Karlsson, R., Latrobe, A., Martin, A., Muhlbauer, P., Scheuerer, M., Smith, B., Takacs, T., Willemsen, S., 2001, “CFD Best Practice Guidelines for CFD Code Validation for Reactor-Safety Applications”, European Comission. ECORA,

[18] Yang H.Q., Singhal A.K., Megahed M. “*The Full Cavitation Model*”. Von Karman Institute for Fluid Dynamics, Lecture Series 2005-04, May 2005

[19] Singhal A.K.,Athavale M.M., Li H., Jiang Y. “*Mathematical Basis and Validation of the Full Cavitation Model*”. Journal of Fluids Engineering. 2002. Vol. 124, pp. 617-624

[20] Nurick, W.H. “*Orifice Cavitation and its Effect on Spray Mixing*”. Jounal of Fluids Engineering. Vol 98. pp 681-687.

[21] http://www.engineeringtoolbox.com/air-solubility-water-d_639.html

[22] http://www.mpch-mainz.mpg.de/~sander/res/henry.hmtl

[23] Menter, F.R., Rumsey, C.L., “Assesment of Two-Equation Turbulence Models for Transonic Flows”, AIAA 94-2343, Proc. 25th Fluid Dynamics Conference, Colorado Springs, Colorado, U.S.A., 20.-23. Juni 1994

[24] Wilcox, D.C., 1988, “Reassesment of the Scale-Determining Equation for Advanced Turbulence Models”, AIAA J., Vol. 26, S. 1299-1310

[25] Wilcox, D.C., 2000, “Turbulence Modelling for CFD”, DCW Industries

[26] Jones, W. P.; Launder, B. E. The Calculation of Low-Reynolds- Number Phenomena with a Two-Equation Model of Turbulence. International Journal for Heat and Mass Transfer 1973,16, 1119.

[27] Spalart, P.R., Shur, M.L., 1997, „On the sensitization of turbulence models to rotation and curvature”, Aerospace Science and Technology, Vol. 1-5, S. 297-302

[28] Frank, T., Lifante, C., Rieck, K, 2007, „CFD Simulation of Cloud and Tip Vortex Cavitation on Hydrofoils”, *Proceedings of the International Conference on Multiphase Flow*. ICMF 07, Leipzig.

[29] Lifante, C., Frank, T., Rieck, K, 2007, “Investigations of Pressure Fluctuations caused by Turbulent and Cavitating Flow around a P1356 Ship Propeller“, *Proceedings of the ANSYS Conference & 25 CADFEM Users Meeting*. ACUM07. Dresden.

[30] Lifante, C., Frank, T., Kuntz, M, 2007, „Extension and Validation of the CFX Cavitation Model for Sheet and Tip Vortex Cavitation on Hydrofoils", *5th Joint FZR & ANSYS Workshop "Multiphase Flows: Simulation, Experiment and Application"*, Dresden.

[31] Anschau, P. Mach, K-P., Rieck, K. 2007, „Stereo PIV measurements for CFD Validation". *Proceedings of the ANSYS Conference & 25 CADFEM Users Meeting*. ACUM07. Dresden.

[32] www.sensoren.de/drucksensoren.htm

[33] ANSYS Inc., 2007, ICEM-CFD 12.0 "Users Manual"

[34] ANSYS Inc., 2007, ANSYS CFX 12.0 "Users Manual".

[35] Schneiders, R., Schindler, R., Weiler, F., 1996, "Generation of Hexahedral Element Meshes". *Proceedings of the 5th International Meshing Roundtable*, Pittsburgh, USA.

[36] Wilcox, D.C., 1988, "Reassessment of the Scale-Determining Equation for Advanced Turbulence Models", *AIAA J.*, Vol. 26, S. 1299-1310

[37] Langtry, R., Menter, F., 2005, "Transition Modeling for General Applications in Aeronautics", *AIAA*, paper 2005-522

[38] Wilcox, D.C., 1986, "Multiscale model for turbulent flows", In *AIAA 24th Aerospace Sciences Meeting*. American Institute of Aeronautics and Astronautics,